FISEVIED

## Contents lists available at ScienceDirect

# Acta Materialia

journal homepage: www.elsevier.com/locate/actamat



# Full length article

# High-throughput exploration of the WMoVTaNbAl refractory multi-principal-element alloys under multiple-property constraints

Brent Vela<sup>a,\*</sup>, Cafer Acemi<sup>a</sup>, Prashant Singh<sup>b</sup>, Tanner Kirk<sup>a</sup>, William Trehern<sup>a</sup>, Eli Norris<sup>a</sup>, Duane D. Johnson<sup>b,c</sup>, Ibrahim Karaman<sup>a</sup>, Raymundo Arróyave<sup>a</sup>

- <sup>a</sup> Department of Materials Science and Engineering, Texas A&M University, College Station, TX 77843 USA
- <sup>b</sup> Ames National Laboratory, U.S. Department of Energy, Ames, IA 50011 USA
- <sup>c</sup> Department of Materials Science & Engineering, Iowa State University, Ames, IA 50011 USA

#### ARTICLE INFO

#### Keywords: Multi-principal element alloys High-temperature materials High entropy alloys Refractory materials High throughput alloy design

#### ABSTRACT

Development of next-generation gas turbines requires the design and fabrication of novel high-temperature structural materials capable of operating beyond 1300°C. We propose a high-throughput alloy design framework under multiple-property constraints to discover new refractory multi-principal element alloys (MPEAs) for high-temperature applications. The framework treats the development of MPEAs as a composition-agnostic constraint satisfaction problem, i.e., no prescriptions are made concerning the design space before performing investigatory calculations. We target alloys in the WMoVTaNbAl chemistry space that are predicted to meet constraints on the following properties simultaneously: single-phase stability, density, solidus temperature, yield strength at 1300°C, and ductile-to-brittle-transition temperature. These properties are relevant to both applications in gas turbines and manufacturability. A set of 214 MoNbV-rich alloys meet these relevant constraints. These feasible alloys are investigated with density functional theory (DFT) to provide a fundamental electronic basis for their superior properties. Three compositionally representative alloys from the feasible design space  $(Mo_{45}Nb_{35}Ta_5V_{15}, Mo_{25}Nb_{50}V_{20}W_5, \text{ and } Mo_{30}Nb_{35}Ta_5V_{25}W_5)$  are selected with a k-medoids-based design scheme for detailed DFT analysis and experimental characterization. The DFT analysis predicted a single-phase BCC at high temperatures with a high yield strength for all three MPEAs, in agreement with CALPHAD (CALculation of PHAse Diagrams) and experiments, respectively. These three alloys are benchmarked against a public database of 1546 MPEAs. Concerning the aforementioned constraints, the Mo<sub>30</sub>Nb<sub>35</sub>Ta<sub>5</sub>V<sub>25</sub>W<sub>5</sub> alloy outperforms these 1546 MPEAs. The present work demonstrates the ability of the proposed design methodology to identify candidate alloys for a given application under multiple property constraints in a combinatorically vast design space.

# 1. Introduction

The current state-of-the-art materials used for gas-turbine engine blades are single-crystal Ni-based superalloys. Modern Ni-base superalloys such as the 4<sup>th</sup>-generation single-crystal CMSX-4® Plus can withstand extreme mechanical stresses (~820 MPa) at temperatures approaching 950°C [1]. However, improvements in the efficiency of gas turbine engines have plateaued, caused partly by inherent limitations in the high-temperature properties of these superalloys [2]. Therefore, novel structural materials capable of operating at much higher temperatures while simultaneously being easily manufacturable are needed to supersede Ni-based superalloys and improve the efficiency of jet

turbine engines. A paradigm shift, namely high-entropy alloys (HEAs), has been proposed to meet this design challenge [3,4].

High-entropy alloys (HEAs) consist of 4 or more principal alloying components with concentrations ranging from 5 to 35 at.% [4,5]. A further generalization of these alloys are multi-principal element alloys (MPEAs), which are similar to HEAs but do not have strict prescriptions for configurational entropy, as is the case with HEAs. While the MPEA space, in general, is broad [4], the search domain can be narrowed by considering certain manifolds of the composition space [6]. A manifold of interest for high-temperature aerospace applications is the refractory MPEA space [7]. Of particular interest to the design problem in question, the equimolar refractory high entropy alloys (RHEAs) NbMoTaW and

E-mail address: brentvela@tamu.edu (B. Vela).

<sup>\*</sup> Corresponding author.

VNbMoTaW have been shown to possess a single-phase BCC crystal structure at high temperatures [8]. Furthermore, these two alloy systems have exceptional high-temperature yield strength exceeding 400 MPa at 1600°C, thus outperforming current state-of-the-art Ni-based superalloys, which have been reported to possess yield strengths below 200 MPa at 1000°C [9]. This indicates that the NbMoTaW or VNbMoTaW alloy systems may contain alloys capable of replacing Ni-based superalloys in jet engine turbine applications.

Regarding the consideration of V in the alloy design space, in an *abinitio* study, Hu et al. [10] showed that the equimolar addition of V to NbMoTaW resulted in 1) shortening of the pseudo-energy gap, which decreased covalent bonding and increased metallic bonding in the alloy, and 2) increased the overlap of the electron clouds between Mo and W enhancing their interaction force and increasing the yield strength in the alloy. These studies indicate that the VNbMoTaW alloy space likely contains alloys capable of maintaining yield strength at extreme temperatures.

Non-refractory metals (Al, Si, Co, Ni, Ti) have been added to refractory MPEAs in order to enhance certain properties such as yield strength [11,12], ductility [13], low density [14,15], and oxidation resistance [11,16,17]. For example, Li et al. [17] showed that the Ti-rich Ti<sub>42</sub> 5Zr<sub>42</sub> 5Nb<sub>5</sub>Ta<sub>10</sub> exhibited mixed passivation films consisting of TiO<sub>2</sub>, ZrO<sub>2</sub>, Nb<sub>2</sub>O<sub>5</sub>, and Ta<sub>2</sub>O<sub>5</sub>. Similarly, Han et al. [13] showed that additions of Ti ductilized the NbMoTaW RHEA. Guo et al. correlated Si additions with decreased density and increased high temperature hardness within the NbTaWMoSi<sub>x</sub> system (where x = 0, 0.25, 0.5, 0.75) [18]. Of particular interest is Al. The addition of Al to refractory MPEAs has shown to have multifaceted benefits. Addition of Al ( $\rho = 2.702$  g/cc) has been shown to reduce the density [11,14] and increase room-temperature and high-temperature yield strength of RHEAs via solid-solution hardening [14,19]. In addition, the inclusion of modest amounts of Al in HEAs has been shown to increase the oxidation resistance via the formation of protective oxides [11,16]. For example, Ge et al. added Al to the MoNbTaTiV system and discovered the resulting alloy possessed improved oxidation resistance [11]. Of particular interest to this work, Kustas et al. [15] developed the ultra-light ultra-hard Al<sub>42</sub>Ti<sub>25</sub>Nb<sub>13</sub>Zr<sub>8</sub>Mo<sub>8</sub>Ta<sub>4</sub> MPEA. This MPEA has a Vicker's hardness of 10-15 GPa and density of 5.7 g/cc. Based on these two measurements the specific strength of the alloy is estimated to be on the order of 1.8-2.6 GPa-cc/g. This alloy is predominately rich in Al (42 at.%). The authors attributed the exceptional specific strength of Al<sub>42</sub>Ti<sub>25</sub>Nb<sub>13</sub>Zr<sub>8</sub>Mo<sub>8</sub>Ta<sub>4</sub> to 1) the large Al content which decreases the density of the alloy and 2) the refractory high entropy nature of the alloy which can potentially increase strength. Specifically, the strength of the alloy was attributed to local compositional variations which are common in refractory MPEAs [20]. These local compositional variations can increase the activation energy barrier for screw dislocation motion, which in turn can promote non-screw dislocation nucleation and glide along various slip planes [15,20,21]. The aforementioned studies indicate that the WMoVTaNbAl alloy space potentially contains refractory MPEAs that may supersede Ni-based superalloys as structural materials in jet turbine engine applications.

Regarding alloy design frameworks, several different methods have been previously utilized for the design of MPEAs. For example, Waseem [22] deployed a combinatorial design of experiments within the  ${\rm Al_x}$ -CryMozNbTiZr alloy space where x,y, and z were varied at increments of 10 at.%. However, this design scheme is not composition-agnostic as the design space was limited to variations of Al, Cr, and Mo. Furthermore, the search space was restricted to 12 potential designs prior to performing any calculations, whereas, if all elements were varied at increments of 5 at.% considering binary to quinary systems, the total number of candidate designs would be 53,124.

Likewise, Feng et al. [23] performed high-throughput (HTP) design of lightweight HEAs for application in aircraft engines within the Al-Cr-Fe-Mn-Ti alloy space. The authors used a constraint satisfaction design scheme to filter 3,246 potential designs to 8 feasible candidate

alloys. However, the constraints used to filter the design space only ensured formation of a BCC phase with L $2_1$  precipitates and did not account for performance metrics such as yield strength. Furthermore, their alloy design scheme was defined such that alloying components could only vary in concentration from 0 to 50 at.%. Additionally, all candidate alloys were required to be quinary, avoiding the larger MPEA space in favor of the RHEA space. This limits the number of candidate designs from 10,621 alloys if binaries to quinaries were considered and compositions were allowed to vary from 0 to 100% to only 3,246 candidate compositions, 30.6% of the original space.

Of particular interest to the present work, Singh et al. [24] used a composition agnostic approach to design MPEAs within the MoWTaTiZr system using a combination of extended Hume-Rothery criteria, density functional theory (DFT), and short-range order (SRO) analysis. While these alloys were designed to be high-strength, they were not screened based on performance metrics relevant to a particular engineering application nor was an explicit prediction of yield strength reported. Furthermore, the authors screened for high strength but did not make considerations for other important properties, such as density or ductility. Alloy design cannot be myopic and must account for multiple constraints and objectives.

Here we seek to take a composition-agnostic and problem-oriented approach to designing MPEAs. First, in our design formulation, we specify performance targets, i.e., material integrity during operation in jet turbine engine blades at 1300°C. We then specify the properties necessary to realize such performance. Next, we conduct an HTP filtering of the MPEA space using analytical and CALPHAD-based (CALculation of PHAse Diagrams) models to down-select alloys that have properties likely to enable the desired performance. The down-selected alloys are then investigated with DFT and SRO analysis to further explain the origin of their superior properties. Finally, using sparse sampling techniques, three alloys are selected to investigate the down-selected MPEA space experimentally.

Regarding sparce sampling of chemical spaces, Khan et al. [25] performed a constraint satisfaction design scheme within the FCC CoCrFeMnNiV-Al system, narrowing the number of candidate alloys from 1,000,000 potential designs to just 398 for further analysis with DFT with the ultimate goal of creating a machine-learning surrogate model capable of predicting stacking fault energies. To better train their surrogate, in addition to the 398 alloys that satisfied all constraints, 100 alloys representing the portion of the alloy space that failed to meet the specified constraints were selected with k-medoids sampling. K-medoids clustering is an unsupervised machine-learning technique that groups objects in a feature space according to a defined metric of distance [26]. Following Khan et al., K-medoids clustering can be used as a space-filling technique, where a design space is discretized into k clusters and the medoids of these clusters are taken as representative members of their clusters. Such a method is preferable to a random sampling as it is guaranteed to generate representative samples of large design spaces via ensuring all feasible candidates represented in the sampled set, which is guaranteed with random sampling, especially sparce-sampling conditions [27].

Here, we remedy the aforementioned shortcomings within a single framework consisting of three steps: (1) HTP composition agnostic multi-constraint factorial exploration of a refractory MPEA space to filter for feasible alloys; (2) DFT analysis on resultant feasible space to explain the fundamental atomic and electronic underpinning for the superior properties associated with the feasible alloys; (3) K-medoids sampling to draw representative samples from the feasible space to further down select viable alloys such that SRO analysis and fabrication and experimental characterization can be performed.

Specifically, we conduct an HTP composition-agnostic factorial exploration of the WMoVTaNbAl MPEA space under constraints relevant to gas-turbine engine applications. We query a suite of CALPHAD, analytical, and machine-learning models in an HTP manner for 53,124 candidate alloys, identifying 214 alloys that simultaneously meet all

design constraints. Using DFT calculations, the electronic origins of high-temperature phase stability and origins of yield strength are explored within these 214 down-selected alloys. Using a design of experiments based on k-medoids sampling, three alloys that best represent the feasible, down-selected composition space ( $Mo_{45}Nb_{35}Ta_5V_{15}$ ,  $Mo_{25}Nb_{50}V_{20}W_5$ , and  $Mo_{30}Nb_{35}Ta_5V_{25}W_5$ ) are selected for further analysis with experimental characterization. Finally, the three alloys are synthesized and characterized in as-cast and homogenized states to assess microstructure, phase constitution, density, and high-temperature yield strength, demonstrating that the selected alloys meet the design specifications. Computational results are then corroborated with experimental validation of the three selected alloys. Furthermore, when application-relevant constraints are considered, we show that only a tiny fraction of the initial refractory MPEA design space (0.54%) remains feasible, a more tractable space for decision-making and design.

The properties of these 3 down-selected alloys are then bencmarked against a public database of 1546 MPEAs reported in literature. Of these 1546 MPEAs, only 2 alloys (MoNbTi [28] and MoNbTaTiV [29]) meet the phase, DBTT, solidus, and density constraints applied in this work. Regarding the yield strength constraint, of these 2 alloys, only MoNbTi has high temperature yield strength data reported up to 1200°C. The best performing alloy design in this work (MoNbTaVW) has a yield strength of 480 MPa at 1300°C, 156 MPa greater than the yield strength of the second best performing alloy (MoNbTi) at 1200°C.

## 2. Computational methods

HTP Property Models: In line with a composition-agnostic design scheme, the initial design space considers all alloys within the WMoV-TaNbAl system and subsystems without any prior preference for particular regions in the design space. Specifically, the aforementioned constraints were queried at increments of 5 at.% considering binary to quinary systems, resulting in 53,124 candidate alloys in total. As this is a vast design space, any models used in such a design scheme must be capable of being queried in an HTP manner. For each of the 53,124 candidate compositions, material properties were predicted in an HTP manner to determine alloy feasibility for high temperature, lightweight, and high strength applications. CALPHAD modeling was used to predict phase stability, density, and solidus temperature. Specifically, equilibrium simulations were conducted for each composition using Thermo-Calc's TCHEA4 database [30]. The high-temperature yield strength was estimated using an analytical model developed by Maresca and Curtin [31] based on the theory that strength in refractory MPEAs is dictated by the glide of edge dislocations through random solute fields. For HTP screening, the lattice parameters, elastic constants, and solute misfit volumes are approximated with rule-of-mixture approximations as recommended by the authors of the model. Details on the implementation of this model are provided in the Supplemental Materials. The Ductile to-Brittle Transition Temperature (DBTT) was estimated with a sure independence screening and sparsifying operator (SISSO) model that was fit to experimental data captured in an in-house database consisting of the DBTT of refractory alloys. Additional details on the DBTT model used in this work can be found in the Supplemental Materials.

Sampling Strategy: Once the feasible design space was identified, using a K-medoids-based sampling technique, compositionally representative alloys were chosen from this down-selected space. K-medoids clustering is similar to the more well-known K-means clustering in that cluster centroids are distributed to minimize intra-cluster variance [26]. However, K-medoids differs from K-means in that centroids must be members of the cluster, whereas, in K-mean clustering, the centroid need not be present in the data set [26]. Furthermore, k-medoids sampling goes beyond clustering, making use of the fact that the selection of medoids can be used as a space-filling technique where a design space is stratified into k clusters, and medoids are taken as representative members of their respective clusters. In design of experiments, such space-filling techniques are preferable to random sampling as they

typically first stratify the design space; samples are then drawn from each strata guaranteeing each stratum is represented, which is not guaranteed with random sampling [27].

Furthermore, a K-medoids-based design of experiments is more appropriate for alloy design than other space-filling techniques, such as the popular Latin hypercube sampling technique. This is because Latin hypercube sampling equally stratifies the design space, and this stratification is *unaware* of the compositions in the feasible design space. On the other hand, the results from k-medoids sampling are defined in a manner that is *composition-aware*. Because of this, the sampling results from k-medoids sampling are more interpretable as the strata from which the medoids were drawn correspond to alloy classes present in the feasible space. Furthermore, k, the number of samples drawn, can easily be specified according to experimental resources. In this case, three compositionally distinct clusters (k = 3) of feasible alloys were defined via k-medoids clustering.

Density functional theory (DFT) calculations: Phase stability (formation enthalpy) and mechanical properties (bulk moduli) were determined using an all-electron, Green's function Korringa-Kohn-Rostoker (KKR) electronic-structure method [32]. The configurational averaging to tackle chemical disorder is handled using the coherent-potential approximation (CPA) [32], and the screened-CPA was used to address Friedel-type charge screening [33]. Valence electrons and shallow lying core electrons affected by alloying are addressed via a scalar-relativistic approximation (where spin-orbit terms only are ignored) [32-34], whereas deep lying core is addressed using the full Dirac solutions. The interstitial electron contributions to Coulomb energy are incorporated using Voronoi polyhedral [34]. The generalized gradient approximation to DFT exchange-correlation was included using the libXC opensource code [35]. Brillouin-zone integrations for self-consistent charge iterations were performed on 24  $\times$  24  $\times$  24 Monkhorst-Pack k-mesh [36]. The charge density is obtained from the function using a complex-energy contour integration using a Gauss-Laguerre quadrature (with 24-point semi-circular mesh enclosing the bottom to the top of the valence states).

Chemical SRO Analysis: A detailed understanding of SRO provides useful guidelines for phase formation and strengthening behavior due to changes in ordering arising from varying chemical compositions in MPEAs [37]. Notably, the chemical ordering in refractory MPEAs is difficult to achieve due to slow atomic diffusivity. However, the presence of SRO could potentially influence thermodynamic [37] and physical properties (strength and creep behavior [38,39]), which is critical for long-term applications. Therefore, the SRO of selected MPEAs was analyzed using linear-response theory [31] that uses self-consistently converged potentials and charge density from KKR-CPA [31]. The linear-response theory directly provides the chemical stability matrix  $(S_{\mu\nu}^{(2)}(k;T))$  and Warren-Cowley SRO parameters  $(\alpha_{\mu\nu}(\mathbf{k};T))$  of all atomic pairs  $(\mu - \nu)$  in the reciprocal space [31]. The SRO was calculated from the relation  $-\alpha(\mathbf{k})_{\mu\nu}^{-1} = c_{\mu}(\delta_{\mu\nu} - c_{\nu}) \left[ \left( \frac{\delta_{\mu\nu}}{c_{\mu}} + \frac{1}{c_{\nu}} \right) - \beta S_{\mu\nu}^{(2)}(\mathbf{k};T) \right]$ , where  $\beta^{-1} = k_B T$ ,  $(c_{\mu}, c_{\nu})$  is composition of  $(\mu, \nu)$ ,  $\delta_{\mu\nu}$  is Kronecker delta function, k is wave-vector, T is temperature, and  $k_B$  is Boltzman constant. For a dominant wavevector  $(k = k_0)$ , the spinodal temperature  $(T_{sp})$  signifies an absolute instability to chemical fluctuations  $(c_{\mu}, c_{\nu})$ , which provides an estimate for order-disorder  $(T_{o-d})$  or miscibility gap  $(T_{MG})$  temperature. For N>2, pairs driving ordering (or clustering) will not necessarily be the same pairs that exhibit peaks in the SRO (due to the matrix inversion implicit above) [31]. Dominant pairs driving SRO are identified from curvature (2<sup>nd</sup>-variation in concentration) of the KKR-CPA electronic grand potential (giving the interchange energies for all pairs), yielding energy cost for concomitant fluctuations  $c_{\mu}, c_{\nu}$  at  $T_{sp}$ . The  $S_{\mu\nu}^{(2)}(k;T)$  of the homogeneously random alloy was determined by including all electronic effects (band-filling, electrostatics. exchange-correlation, hybridization, Fermi-surface, and van Hove states) [40,41] The SRO calculations can also identify the favorable SRO modes, the associated energy gain, the atomic pairs driving a possible phase transition, and its electronic origin [37], offering direct insight into the ways to tune the materials behavior.

Visualization of Design Space: In Refs. [25,42,43], the authors visualize compositional-property relationships in high-dimensional alloy spaces by projecting a uniformly sampled compositions space to 2-dimension using t-distributed stochastic neighbor embedding (t-SNE) [44]. t-SNE is an unsupervised machine-learning non-linear dimensionality reduction technique that can preserve global and local structure of high-dimensional data after projection to a lower dimension. In summary, t-SNE maps Euclidean distances in high-dimensional space to Gaussian distributions, creating joint probability distributions that represent the similarities between every possible pair of points in the dataset. The high-dimensional space is randomly projected to two dimensions, and in a similar manner, Euclidean distances in low-dimensional spaces are mapped to Cauchy distributions. Finally, the Kullback-Leiber divergence between the joint probability distributions in both high-dimensional and low-dimensional space is minimized by iteratively rearranging the position of points in the low-dimensional embedding [44].

In this work, we take a similar approach. We rely on the uniform manifold approximation and projection (UMAP) dimensionality reduction technique [45]. UMAP is also an unsupervised machine-learning non-linear dimensionality reduction technique. By assuming that data is uniformly distributed on a locally connected Riemannian manifold [45], UMAP uses local manifold approximations to create a fuzzy topological representation of a high-dimensional space. A low-dimensional representation of the space is then iteratively optimized to have as close a fuzzy topological representation as possible as measured by cross entropy. UMAP has been shown to better preserve both global and local structure in data than t-SNE is able to. This is reflected in the resultant projections of the alloy space. More comparisons between t-SNE and UMAP are discussed in the Supplementary Materials associated with this work.

## 3. Experimental methods

Three designed refractory MPEA compositions were synthesized from high-purity elements (>99.9 wt.%) using a Buehler AM200 vacuum arc melter (VAM) under an Ar atmosphere. Each coupon was flipped and remelted 10 times to ensure homogeneity of the alloys. The lightest element in the candidate alloys, V, was added to the melt last to reduce loss due to evaporation during fabrication. Homogenization heat treatments were performed using a Centorr high temperature furnace (LF Series, Model 22) under an Ar atmosphere by purging the chamber 3 times before the heat treatments. After the heat-treatments, the candidate alloys were furnace-cooled down to room temperature. The selection of heat treatment time and temperature was guided by the Thermo-Calc's Diffusion Module (DICTRA). These calculations were based on the time required for alloying components to diffuse and eliminate compositional differences between the dendritic and inter-dendritic regions, and dendrite arm spacing (DAS). The Archimedes method was employed to measure the densities of the arc melted coupons after heat treatments by using an analytical balance equipped with a density determination kit and ethanol ( $\rho = 0.789 \text{ g/cm}^3$ ) as an immersion liquid. Sample profiles were then cut via wire electrical discharge machining (wire-EDM) to produce compression specimens with a diameter of 6 mm and height of 9 mm, and a cross-sectional slice for electron microscopy (SEM/EDX), X-ray Diffraction (XRD), Vickers Microhardness, and nanoindentation. The cross-sectional slices were polished using abrasive SiC polishing papers to produce a final polish of 15  $\mu m$ , then placed into a vibratory polisher for 48 h in 0.04  $\mu m$  colloidal silica suspension. The samples were ultrasonicated for 15 min in an isopropanol bath at  $50^{\circ}\text{C}$  to clean the surface and remove any residual solution before microstructural investigation.

The microstructure of the samples was investigated using FEI Quanta  $600\,$  FE-SEM with a voltage of 20kV. An Oxford Instruments energy

dispersive X-ray spectroscopy (EDS) system equipped with X-ray mapping and digital imaging was used to determine the composition of the dendritic and inter-dendritic regions as well as the average composition of the synthesized alloys. Lattice parameters and phase structures were determined using a Bruker D8 Discover X-ray Diffractometer equipped with a Cu K- $\alpha$  X-ray source and a Vantec 500 area detector. The Vickers microhardness measurements were obtained using a LECO LM-100 Microhardness Tester with an applied force of 500 gf and a dwell time of 20 s by performing at least 10 measurements in each sample following ASTM E92-17 standard. A minimum of ten times of the Vickers diagonal length is used as indentation spacing from the edges and between the indents to obtain hardness measurements along the cross-sectional slices. Room temperature nanoindentation experiments were performed using a Hysitron TI-950 Triboindenter with a maximum load of 10,000  $\mu N$ ; a total of 25 equally distributed indents have been used in a 100  $\mu m$ by 100 µm region. Nanoindentation experiments are performed only after the heat treatments to reduce the uncertainty caused by the dendritic microstructure in the as-cast condition. High-temperature compression experiments were conducted on a Gleeble uniaxial compression setup (Gleeble 3500) at 1300°C with a strain rate of 0.01 s<sup>-1</sup>. Ambient temperature compression experiments are performed using a Material Testing Systems (MTS) servomechanical test frame with a strain rate of  $0.001 \text{ s}^{-1}$ . The 0.2% offset method is used to measure the yield strength values of the materials after the compression experiments.

#### 4. Results and discussion

Design Formulation: The process-structure-property-performance (PSPP) chain is a critical tool in materials design [46]. Specifically, in this work we seek linkages between structure, property, and performance. Candidate materials for applications in gas turbine engines must meet various design constraints that relate the materials structure and properties to predicted performance. Regarding structure, in order to ensure no undesired phases form during operation, we restrict the feasible alloy space to single phase BCC compositions with stability from 1300°C to its solidus temperature. Regarding properties, candidate alloys must be capable of operating at  $1300^{\circ}\text{C},$  therefore, it is required that the solidus temperature associated with these alloys be well above the operation temperature. Following the rule-of-thumb that the maximum operating temperature of an alloy is typically near 2/3 of its melting temperature, an alloy required to operate at 1300°C must have a melting temperature ( $T_{solidus}$ ) of at least 1950°C. We stipulate that feasible alloys must have a  $T_{\text{solidus}} > 2000^{\circ}\text{C}$ . Regarding density ( $\rho$ ), because many gas turbine engines are used in the aerospace industry, candidate alloys must be lightweight. The density  $(\rho)$  of Ni-based superalloys is on the order of 9 - 10 g/cc [47], therefore, we stipulate feasible alloys must have a  $\rho$  < 9 g/cc near their solidus temperature. As mentioned, candidate alloys will be subjected to centrifugal forces and other inherent operating stresses that result in creep [48], and thus, the feasible alloys must have a predicted yield strength at 1300°C ( $\sigma_{vs}^{HT}$ ) greater than 150 MPa. Candidate alloys must have a yield strength at least above the stresses that will be applied at 1300°C creep testing, therefore this yield strength constraint was defined based on the standard temperatures and stresses applied during creep tests, i.e. 137 MPa at 1100°C [49]. For this reason,  $\sigma_{\rm YS}^{\rm HT} > 150$  MPa was defined as the yield strength constraint. The intrinsic brittleness of refractory MPEAs is a known bottleneck in their development and deployment in engineering applications [3]. Regarding manufacturability, to ensure candidate alloys are workable and resistant to cracking at reasonable temperatures, we stipulate that feasible alloys must have a DBTT < 400 K. These constraints (as summarized in Table 1) are used to screen for feasible alloys within the candidate design space. It should be noted that the design constraints described above (and in Table 1) are derived directly from specifications by the Department of Energy's ARPA-E ULTIMATE program [50]. Thus, the present alloy design formulation has practical

**Table 1**Summary of constraints, the number of designs that pass each constraint, and the information source associated with each constraint.

Constraint	N Samples that Pass Constraint	Information Source
$\rho < 9 \text{ g/cc at Solidus}$	14,016	Thermo-Calc Equilibrium Simulation
$T_{solidus} > 2000^{\circ} \text{C}$	24,208	Thermo-Calc Equilibrium Simulation
Single Phase BCC at $1300^{\circ}$ C and $T_{solidus}$	27,284	Thermo-Calc Equilibrium Simulation
$\sigma_{ m YS}^{ m HT} > 150$ MPa at $1300^{\circ}$ C	22,219	Curtin-Maresca Model
DBTT < 400  K	11,053	SISSO-Based Model
All Constraints	214	N/A

#### relevance.

High-Throughput Screening of Refractory MPEAs: Relevant property data was queried for all 53,124 candidate designs. To visualize the relationship between composition and alloy properties in this MPEA system, we project this 5-dimensional alloy space into 2-dimensions using UMAP embedding, as shown in Fig. 1. Alloys of similar composition are mapped closer to each other in the 2-dimensional embedding, however, there is no strictly quantitative relation between the distance separating two points and their compositions. The corners and edges of this hexagonal UMAP correspond to unary and binary compositions, respectively. Ternaries appear closer to corners and edges than quaternaries would appear. The higher the configurational entropy of the alloy, the closer to the center the alloy will be embedded in 2-dimensions. More details about this visualization technique can be found in the Supplementary Materials.

After relevant property data was queried for every composition in the total set of 53,124 candidate designs, constraints were applied to filter for candidate compositions that are predicted to meet constraints relevant to applications in gas turbine engines. In the top row of Fig. 1, candidate alloys that fail a particular constraint are depicted in gray while alloys that meet a specific constraint are colored according to the

value of the property of interest. Alloys that perform well with respect to a particular constraint are depicted in yellow and while alloys narrowly meet a particular constraint are shown in dark purple.

Because Al is typically a minor alloying component in refractory systems to improve oxidation resistance, it is expected that Al-rich regions of the design space would fail the BCC phase stability constraint, as shown in the UMAP projection of the design space in Fig. 1 (A1). In high concentrations, Al destabilizes the BCC phase in alloys within this refractory chemistry space, whereas refractory elements promote the formation of a BCC phase. Furthermore, Fig. 1 (A2) depicts the BCC phase fraction of every candidate alloy plotted against alloy complexity (the configurational entropy prior to scaling with the Boltzmann constant) and colored according to the at.% of refractory elements present in the alloy. Points containing 50 at.% or more of a particular element are colored according to the majority element. Increasing refractory content corresponds to increased stability of the BCC phase. Finally, Fig. 1 (A3) is a scatter plot of BCC phase fraction against Al content. The number density of points is indicated with a superimposed kernel density estimation (KDE). Fig. 1 (A3) demonstrates how increasing Al content decreases the predicted mol fraction of the BCC phase in candidate alloys.

Regions rich in the densest alloying components W and Ta fail the density constraint. This is depicted in Fig. 1 (B1) where alloys in the Tarich and W-rich corners of the UMAP projection fail to meet the density constraint. Furthermore, Fig. 1 (B2) depicts the density of candidate alloys plotted against alloy complexity. The color for each element in B2 matches the color of that element in B1. From this visualization is evident that W-rich and Ta-rich alloys fall well above the density constraint. Finally, the densifying effect of W and Ta is shown in Fig. 1 (B3) where the density is plotted against the concentration of each of these elements. Increasing W and Ta content leads to the violation of the density constraint.

The elements in the alloy space with the lowest melting temperatures are Al and V with the melting temperatures of 660°C and 1910°C, respectively. Thus, regions rich in these two elements fail the solidus temperature constraint, as shown in the UMAP projection of the design

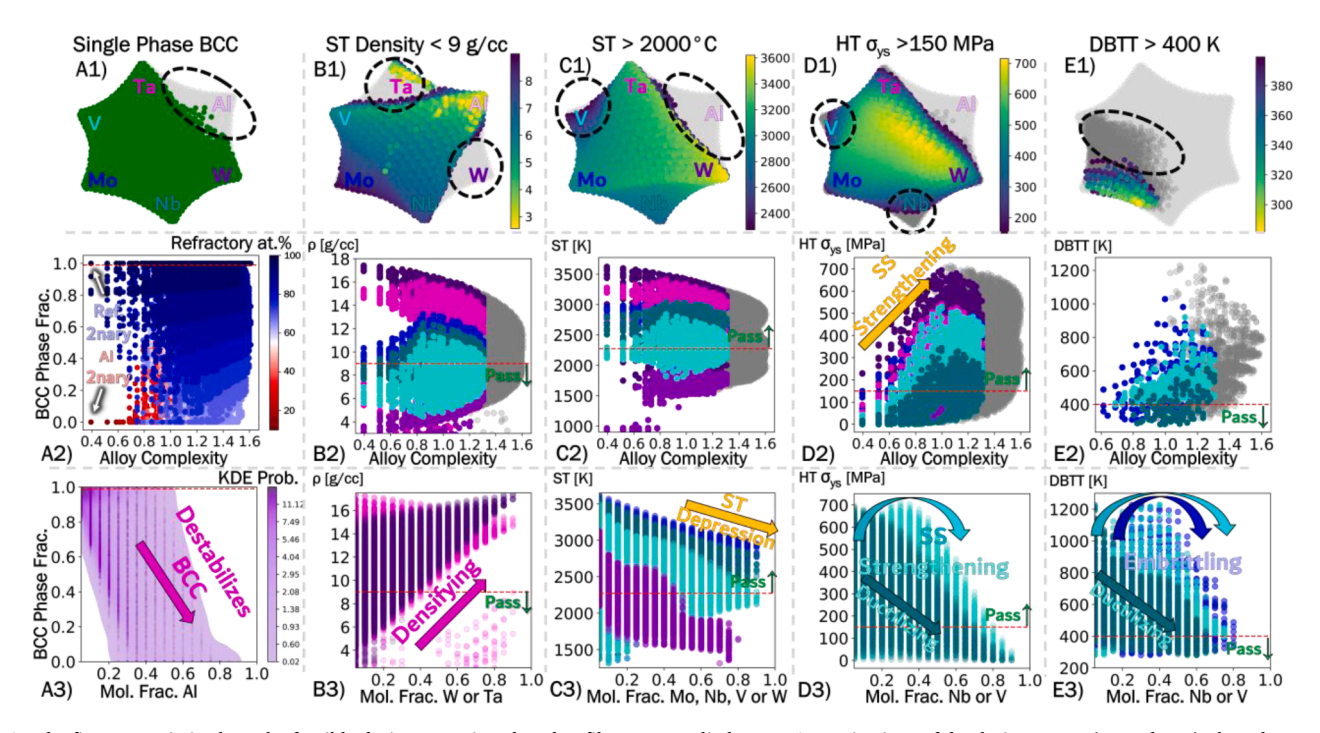


**Fig. 1.** The first row epictins how the feasible design space is reduced as filters are applied on UMAP projections of the design space. (second row) Plotted properties of interest against alloy complexity (unscaled configurational entropy) and uses color as a third axis that depicts compositions greater than 50 at.% of a single element. The second row demonstrates how alloying complexity and composition affect properties of interest. The third row shows the individual effect of alloying additions by plotting the at.% of alloying elements against properties of interest. ST: Solidus Temperature, SS: Solid Solution, HT: High Temperature i.e. 1300°C.

space as shown in Fig. 1 (C1). Elements that contain 50 at.% of V or Al fall below the solidus constraint as shown in Fig. 1 (C2). The melting temperature of V is  $1910^{\circ}$ C, just below the solidus temperature constraint of  $2000^{\circ}$ C. Binary alloys are shown on the left side of the scatter plot whereas more chemically complex alloys are on the right. From this it is evident that additions of elements with higher melting temperature can cause V-rich alloys to pass the solidus constraint. All elements depicted have melting temperature below that of W. Because of this, an increase of any element besides W will cause some degree of melting point depression. This melting point depression is increased with increasing alloy complexity, as can be seen in Fig. 1 (C2). Fig. 1 (C3) shows the individual effect of alloying components on the melting temperature of alloys. An increase in Al and/or V will lead candidate alloys to violate the solidus temperature constraint.

Because the Curtin-Maresca model is only valid for BCC MPEAs, the BCC constraint is applied first, followed by the yield-strength constraint. Alloys that are BCC yet fail the yield strength constraint are depicted as dark grey in Fig. 1 (D1). Regarding yield strength, high-entropy W-rich regions have the highest predicted yield strength, however, these same W-rich regions fail the density constraint. According to Fig. 1 (D2), W-rich binaries have the highest predicted yield strength followed by Morich binaries, Ta-rich binaries, V-rich binaries and finally Nb-rich binaries. As alloy complexity is increased this rank-ordering according to yield strength is preserved, i.e., W-rich MPEAs have the highest

predicted yield strength followed by Mo-rich MPEAs. Fig. 1 (D2) also demonstrates how yield strength increases with increased alloy complexity. This can be attributed to solid solution strengthening as captured in the Curtin-Maresca model. In Fig. 1 (D3), the induvial effect of increasing the concentration of elements is investigated. Nb has a purely ductilizing effect on the alloys and contributes little to solid-solution strengthening. There is an optimum concentration of V that contributes to solid-solution strengthening; This optimal concentration is 25-30 at.% V. Beyond this optimum concentration of V, the yield strength of candidate alloys begins to diminish. These results are in agreement with analysis performed by Yin et al. [51] where they demonstrate that, because of its large atomic mismatch within refractory MPEA lattices, inclusions of V at 25 at.% is optimal for strengthening BCC high entropy alloys.

Because the SISSO-based DBTT model is intended for HTP screening of the alloy space as opposed to high accuracy, we first apply the solidus, density and phase stability constraints, followed by the yield strength constraint. After narrowing the number of candidate compositions, the last constraint applied is the DBTT constraint. In Fig. 1 (E1), alloys that do not pass the four constraints mentioned above are depicted in light gray, whereas alloys that pass these four constraints but do not pass the DBTT constraint are shown in dark gray. According to the UMAP in Fig. 1 (E1), the DBTT constraint removes V-rich regions in the design space. From Fig. 1 (E2), it is clear that upon application of the DBTT

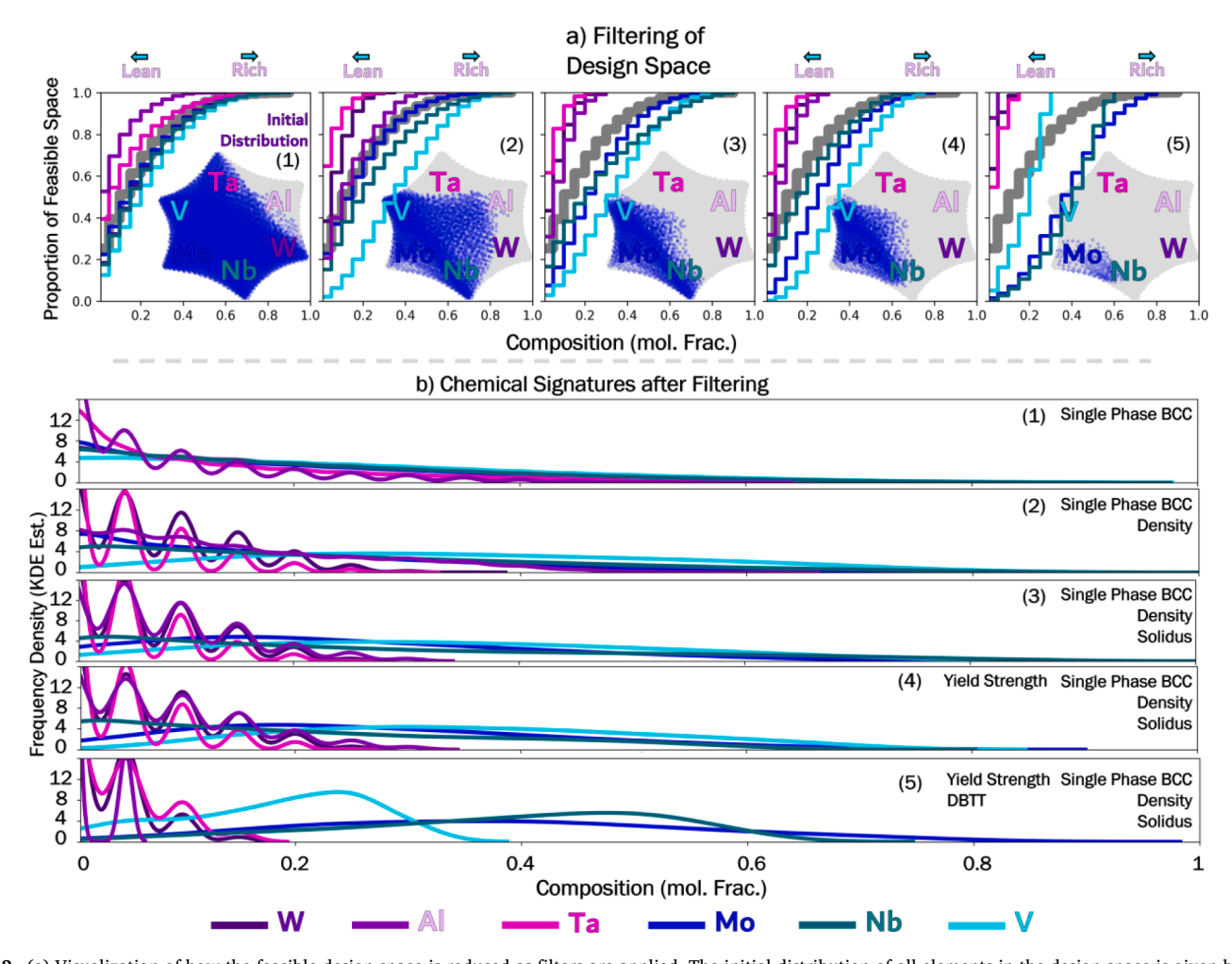


Fig. 2. (a) Visualization of how the feasible design space is reduced as filters are applied. The initial distribution of all elements in the design space is given by the gray line in the empirical cumulative distribution function (ecdf) plots. These ecdf plots depict the proportion of the dataset that falls below each value present in the dataset. As filters are applied, the feasible space is depleted in Al, Ta, and W and enriched in Mo, Nb, and V. (b) Visualization of how the chemical signature of the design space is reduced as filters are applied. The distribution of elements shown as KDE plots fitted over histograms of the concentration of all elements in the design space.

constraint, the space is enriched in the ductile element, Nb. The ductilizing effect of Nb is further seen in Fig. 1 (E3), where Nb causes a monotonic decrease in the DBTT, whereas Mo and V cause embrittlement at concentrations near 20 at.% to approximately 40 at.%.

Table 1 lists each constraint and the corresponding number of satisfactory compositions. When considered individually, no constraint reduces the design space to a tractable number of candidate designs. When all constraints are considered simultaneously, only 0.54% of the initial design space remains feasible. As more constraints are considered, the feasible space becomes richer in MoNbV. This preference for MoNbV-based alloys can be seen in Fig. 2 a(5) as the final feasible set of alloys lies near the MoNbV-rich corners of the UMAP projection.

Upon inspection of the feasible space, we would expect alloys that meet all constraints to be rich in Nb, Mo, and V. For a quantitative analysis, a histogram depicting the relative frequency an element appears in the feasible space at a certain composition can represent the chemical signature of the feasible space as various constraints are applied (Fig. 2). A kernel density estimate (kde) is fit over the distributions and the underlying histograms are removed such that the distributions are more easily visible. In a similar way, empirical cumulative distribution function (ecdf) plots show how various constraints enrich or deplete the feasible space of certain elements. First, the phase stability constraint depletes the feasible space of Al. This can be seen by the Al signature shifting to the left (lean) in the ecdf and kde plots in Fig. 2 a(1) & b(1). The density constraint then depletes the feasible space of Ta and W. This can be seen by the Ta and W signatures shifting to the left (lean) in both ecdf and kde plots in Fig. 2 a(2) & b(2). The solidus constraint then slightly depletes the space of V and enriches the space in Mo as seen in Fig. 2 a(3) & b(3). The yield strength constraint slightly depletes the feasible space of Nb and marginally enriches the space V and Mo, as seen in Fig. 2 a(4) & b(4). Finally, the DBTT constraint depletes the space of V-rich regions and enriches the space in Nb, which is seen in Fig. 2 a(5) & b(5).

In the final down-selected space [Fig. 2 a(5) & b(5)], Mo, Nb, and V signatures are shifted to the right, indicating the feasible alloy space is richer in these three constituents, rather than Al, Ta, and W. The V signature has a more localized peak than the Mo and Nb peaks, indicating that, within the set of feasible alloys, V appears in a narrower range of concentrations (0 to  $\sim\!35$  at.%). The Mo, Nb peaks are broad, indicating the set of feasible alloys contains a wide range of concentrations at which these two elements appear. If W and Ta appear in the feasible space, it will only appear below 20 at. %, and most frequently at 5 at.%. Likewise, if Al appears in the feasible space, it will only appear at 5 at.%.

Sampling from Down-Selected Design Space: From the 214 alloys

satisfying all five constraints, three compositionally distinct clusters of alloys were identified with k-medoids clustering. The medoids of these clusters were selected as representative members of these three compositionally distinct groupings of alloys: Mo-rich MPEAs, Nb-rich MPEAs, and higher entropy quinary MPEAs. The three chosen compositions representing these groups are  $Mo_{45}Nb_{35}Ta_5V_{15}$ ,  $Mo_{25}Nb_{50}V_{20}W_5$ , and  $Mo_{30}Nb_{35}Ta_5V_{25}W_5$ , respectively.

*DFT Analysis of Feasible Design Space*: Within this tractable design space of 214 candidate alloys, DFT is leveraged to understand the fundamental atomic and electronic basis for the superior properties associated with these MoNbV-rich alloys.

In Fig. 3, we plot results from high-throughput DFT analyses of phase stability, intrinsic strength (bulk moduli), and compressive yield strength ( $\sigma_{CS}$ ) for the 214 down-selected MPEAs. The formation enthalpy of the down-elected MPEAs can be divided into V-rich and V-poor regions, as shown in Fig. 3a. In the V-rich case, the  $E_{form}$  decreases with decreasing Mo content. In V-poor region, the  $E_{form}$  first decreases until 45 at.% of Mo, then increases with further increase in Mo. We also found that increasing Mo stabilizes the selected MPEAs, which is reflected in increasing  $E_{form}$  Fig. 3a. Recently, Singh et al. [52] attributed increased phase stability in V-rich alloys to its higher electronegativity compared to other refractories. Therefore, we can conclude that V-reinforced alloys have a higher Mo solubility limit than V-poor cases.

The bulk moduli can be correlated to electronic behavior as electrons can freely move in metals that resist compression due to electronic repulsion [53,54]. Thus, understanding bulk moduli will allow us to understand electronic factors that affect the mechanical properties such as strength. For example, in Fig. 3b, we plot the same V-rich subset of alloys depicted in Fig. 3a. The large bulk moduli of Mo and other group VI elements (Cr,W) arises from the tendency of these elements to pull more valence charges to bonding region that improves the resistance of chemical bonds to compression. Recently, Singh et al. [24] and Vazquez et al. [55] used DFT and machine learning, respectively, to show that more negative  $E_{\rm form}$  directly correlates with higher bulk moduli and strength in refractory MPEAs. This suggests that compositions with higher stability and higher bulk moduli can have a higher probability to have higher strength in MPEAs. Thus, Mo-rich alloys are predicted to have higher yield strengths in this design space.

Temperature dependence of yield-strength and its electronic origin: In Fig. 3c, for the 214 feasible alloys, we plot the temperature-dependent yield strength as predicted with the Curtin-Maresca model using DFT-queried values for lattice parameter, elastic constants, and solute misfit volumes, as opposed to ROM approximations. Points are plotted in increasing order of Mo+V compositions. Our findings indicate that  $\sigma_{YS}$  first increases with Mo+V composition, peaking at an optimal V

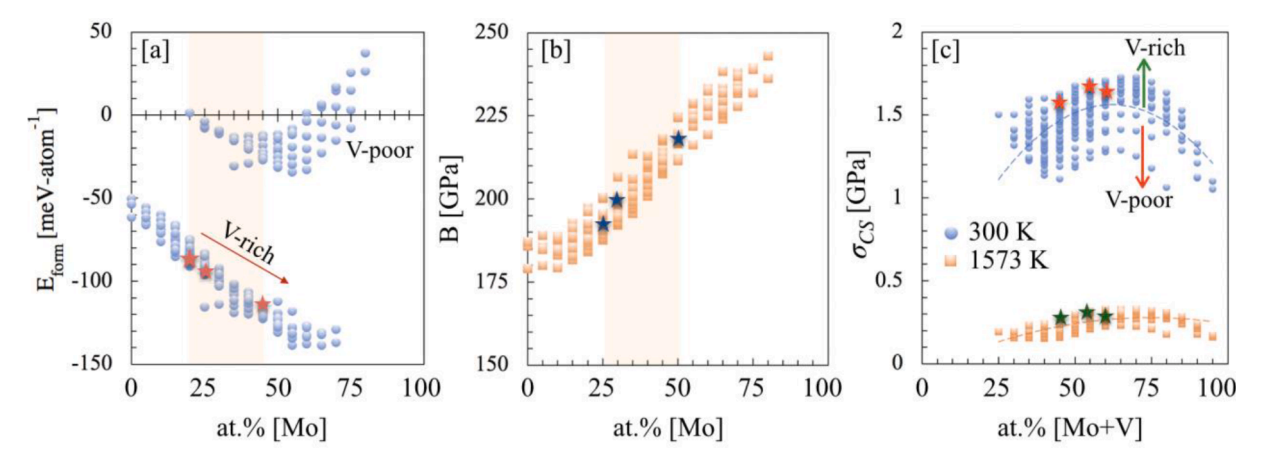


**Fig. 3.** (a) Formation enthalpy (E<sub>form</sub>; meV/atom), and (b) bulk moduli (GPa) of CALPHAD-filtered MoNbV-based alloys are plotted vs. Mo concentration. (c) Compressive strength ( $\sigma_{CS}$ ) is shown at 300 K (blue circles) and 1573 K (orange squares) and increasing Mo at.% shows higher  $\sigma_{YS}$  for V-rich alloys, while lower  $\sigma_{YS}$  for V-poor alloys.

concentration of 15-25 at.%. The DFT-derived  $\sigma_{YS}$  shows a clear divide between V-rich and V-poor regions, emphasizing that for optimal yield strength both Mo and V can be tuned to further improve the phase stability and mechanical properties. The improved chemical and mechanical response of Mo/V rich MPEAs can be attributed to higher Allenscale electronegativity of V compared to other refractories that enables to pull more valence charges into the bonding region from neighboring sites that allows to create strong solid-solution strengthening through local atomic distortions [52].

Origin of Phase Stability of Selected MPEAs: During heating and holding at a testing temperature, MPEAs may experience phase transformations and decompose into a multi-phase structure due to increased chemical correlation [28]. We choose the three MPEAs selected with k-medoids sampling for SRO analysis, i.e.,  $Mo_{45}Nb_{35}V_{15}Ta_5$ ,  $Mo_{25}Nb_{50}V_{20}W_5$ , and  $Mo_{30}Nb_{35}V_{25}W_5Ta_5$ .

In Fig. 4, we plot SRO for  $Mo_{45}Nb_{35}V_{15}Ta_5$  and  $Mo_{25}Nb_{50}V_{20}W_5$  along high-symmetry direction in the BCC Brillouin zone at  $1.15T_{sp}$ ,  $(T_{sp}=$  calculated spinodal decomposition temperature), to understand the ordering behavior. The highest SRO peak for a given pair at a high-symmetry point shows the dominant pair(s) driving phase decomposition in chemically complex alloys. In Fig. 4a, we plot the SRO for BCC  $Mo_{45}Nb_{35}V_{15}Ta_5$  at  $1.15T_{sp}$   $(T_{sp}=945~K)$  that shows competing ordering and clustering peaks at  $k_0=H=[111]$  and  $k_0=\Gamma=[000]$ , respectively. However, ordering peak in Ta-V at  $k_0=H$  is slightly more dominant than clustering peak at  $k_0=\Gamma$ . The dominant SRO Ta-V pair reveals the unstable (Fourier) modes with ordering wave vector  $(k_0)$  at  $T_{sp}$ .

Similar to Fig. 4a, we plot SRO for  $Mo_{25}Nb_{50}V_{20}W_5$  and  $Mo_{30}Nb_{35}V_{25}W_5Ta_5$  in Fig. 4b & c, which show increasing SRO strength from 1.21 Laue (Ta-V pair) to 2.33 Laue (Ta-W pair) with increasing V from 15 to 25 at.% The increasing SRO strength is suggestive of increased bonding strength in alloys due to increased local chemical interaction, which is expected to result in higher strength. Our predictions are in agreement with the recent finding of Beniwal et al. [56] that demonstrates direct correlation of SRO with increasing hardness in MPEAs. The SRO pair with peak at H-point in BCC Brillouin zone shows ordering interaction with B2-type SRO (phase change below  $T_{\rm sp}$ ) for all three MPEAs [37]. The higher stability and increasing trends of  $T_{\rm sp}$  with increasing complexity indicates single-phase BCC formation at high temperature for  $Mo_{45}Nb_{35}V_{15}Ta_5$ ,  $Mo_{25}Nb_{50}V_{20}W_5$ , and  $Mo_{30}Nb_{35}V_{25}W_5Ta_5$  MPEAs.

Microstructural Investigation of Selected Alloys: In as-cast form, all synthesized alloys have a dendritic microstructure, as observed in the Back-Scattered Electron (BSE) images in Fig. 5. EDX compositional analysis is performed on the dendritic and inter-dendritic regions to determine the compositional difference (given in Table 2) and EDS maps were generated for each alloy at a higher magnification to better visualize the dendritic segregation by element. Segregation of the low-melting-point elements, Nb and V, into the inter-dendritic regions is observed where the dendritic regions are rich in high-melting-point elements, Mo, Ta, and W. The average dendrite arm spacing for the synthesized alloys are: 12.8 ( $\pm 4.8$ )  $\mu$ m, 15.1 ( $\pm 2$ )  $\mu$ m, and 13.4 ( $\pm 2.2$ )  $\mu$ m

for  $Mo_{45}Nb_{35}Ta_5V_{15}$ ,  $Mo_{25}Nb_{50}V_{20}W_5$ , and  $Mo_{30}Nb_{35}Ta_5V_{25}W_5$ , respectively. Complete chemical homogenization has been achieved after 1925°C at 12 h heat treatments and confirmed with the EDS line scans, which can be seen in Fig. 6.

Phase Identification of Selected Alloys: Room-temperature XRD is performed to identify the phases present in the materials in as-cast form and after the heat treatments, as shown in Fig. 7. As previously reported [57], multiple BCC phases can be observed in as-solidified refractory MPEAs because of the compositional dissimilarity between the dendritic and inter-dendritic regions. In this study, two BCC phases with slightly different lattice parameters have been identified with XRD for two alloy compositions in the as-cast form  $(Mo_{45}Nb_{35}Ta_5V_{15}$  and  $Mo_{30}N_{15}$ b<sub>35</sub>Ta<sub>5</sub>V<sub>25</sub>W<sub>5</sub>). Elimination of dendritic microstructure via homogenization heat treatments resulted in single-phase BCC structures, which can be seen in Fig. 7. Given the small number of grains present in the scanned area with XRD, the texture effects, more noticeably in homogenized conditions, might affect the different relative intensities of the identified peaks. Lattice parameters of the present BCC phases after heat treatment are measured as follows: 0.318 nm, 0.316 nm, and 0.318 nm for  $Mo_{45}Nb_{35}Ta_5V_{15}$ ,  $Mo_{25}Nb_{50}V_{20}W_5$ , and  $Mo_{30}Nb_{35}Ta_5V_{25}W_5$ , respectively. The candidate alloys were predicted to have a single BCC phase at 1300°C using CALPHAD; the XRD results confirm the predicted crystal structure after the homogenization. Furthermore, the lattice parameters of the alloys are predicted using DFT as follows: 0.315 nm, 0.316 nm, and 0.314 nm for Mo<sub>45</sub>Nb<sub>35</sub>Ta<sub>5</sub>V<sub>15</sub>, Mo<sub>25</sub>Nb<sub>50</sub>V<sub>20</sub>W<sub>5</sub>, and Mo<sub>30</sub>Nb<sub>35</sub>Ta<sub>5</sub>V<sub>25</sub>W<sub>5</sub>, respectively. Experimental results validate the predictions via CALPHAD and DFT for the phases and lattice parameters. A summary of experimental and computational results can be found in

Density of Selected Alloys: After heat treatments, the densities of the three homogenized candidate alloys were measured using the Archimedes method. CALPHAD predictions indicate that the Mo<sub>45</sub>Nb<sub>35</sub>T<sub>5</sub>V<sub>15</sub>,  $Mo_{25}Nb_{50}V_{20}W_5$ , and  $Mo_{30}Nb_{35}Ta_5V_{25}W_5$  alloys would have densities of 9.50 g/cc, 9.13 g/cc, and 9.57 g/cc. The densities measured experimentally for the synthesized alloys are 9.41 g/cc, 9.09 g/cc, and 9.44 g/ cc, respectively. Slightly lower experimental densities were observed due to intergranular and intragranular porosity formation during the synthesis, which reported numerously as a common issue with refractory alloys produced with VAM [3]. Besides the porosity in the as-cast microstructure that occurred during solidification, more porosity formation has been identified after the heat treatments at 1925°C (Fig. 5, pores as dark spots can be seen in homogenized BSE images). This can be explained by the vaporization of the oxide compounds during heat treatment that are trapped in the microstructure during the synthesis, since the evaporation temperatures of the oxides are lower [58] than the heat treatment temperature. However, a more in-depth investigation is required to confirm the main cause of porosity formation during the synthesis and after the heat treatments, which will be investigated in the future publications.

Mechanical Properties of the Designed Alloys: All samples were tested using the Vickers microhardness method at room temperature (Fig. 7) and the average of 10 measurements for as-cast and homogenized

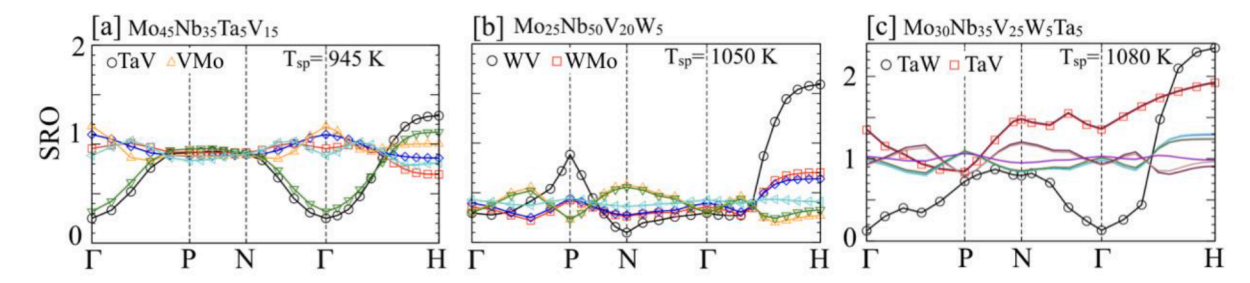


Fig. 4. Short-range order (Laue units) for single-phase MPEAs, i.e., (a)  $Mo_{45}Nb_{35}V_{15}Ta_5$ , (b)  $Mo_{25}Nb_{50}V_{20}W_5$ , and (c)  $Mo_{30}Nb_{35}V_{25}W_5Ta_5$ , plotted along high-symmetry directions in the BCC Brillouin zone at  $1.15T_{sp}$  ( $T_{sp}$ = calculated spinodal decomposition temperature). Marked are pairs that show dominant SRO.

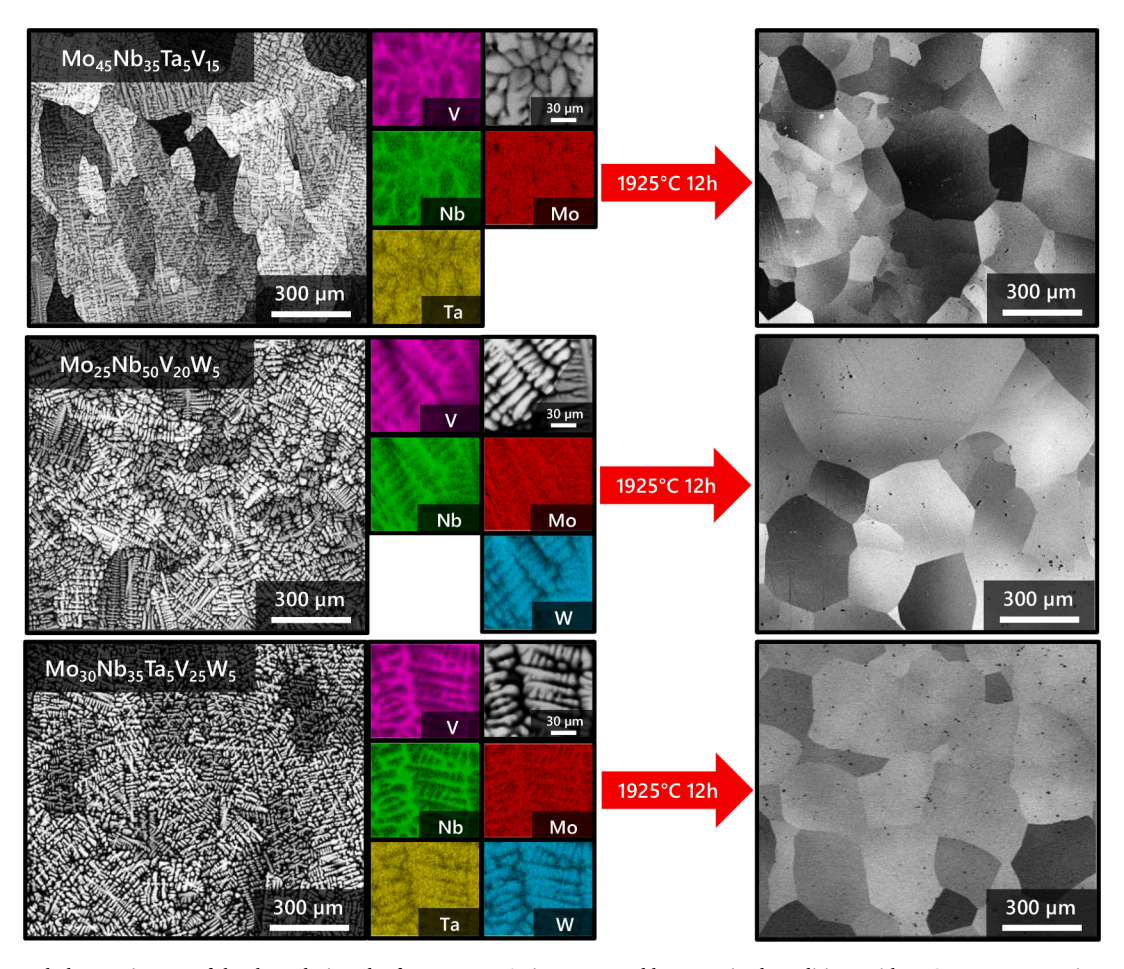


Fig. 5. Backscattered-electron images of the three designed refractory MPEAs in as-cast and homogenized conditions with EDS maps representing each element and relative concentrations in the dendritic and inter-dendritic regions.

conditions are reported in Table 2. The quinary refractory MPEA, Mo<sub>30</sub>Nb<sub>35</sub>Ta<sub>5</sub>V<sub>25</sub>W<sub>5</sub>, exhibited the highest hardness value both in ascast form (520 ( $\pm 8$ ) HV) and after homogenization (480 ( $\pm 16$ ) HV) as compared to the other two quaternary candidate alloys. The present quaternary Mo<sub>25</sub>Nb<sub>50</sub>V<sub>20</sub>W<sub>5</sub> with higher Nb and lower V-W content compared to an equiatomic quaternary MoNbVW alloy produced via VAM (the lattice parameter: 0.3157 nm, hardness: 648 HV in as-cast form [59]), displayed a larger lattice parameter of 0.3208 nm and a lower hardness of 497 ( $\pm$ 7) HV in as-cast form. On the other hand, the explored quaternary alloy Mo<sub>45</sub>Nb<sub>35</sub>Ta<sub>5</sub>V<sub>15</sub> in this study compared to equiatomic quaternary MoNbTaV alloy (the lattice parameter: 0.3208 nm, hardness: 504 HV in as-cast form [60]) exhibited similar hardness response of 503 ( $\pm 9$ ) HV in as-cast. A decrease in the Vickers microhardness responses after the heat treatments was observed for all the synthesized alloy compositions, with an average of 6%. Comparison of the hardness values after homogenization was not possible due to the lack of publications for homogenized refractory alloys in the literature.

The three refractory MPEA compositions were tested in compression for the homogenized condition at ambient temperature and  $1300^{\circ}\text{C}$  (Fig. 8) to determine the yield strength and maximum compressive stress. In addition to high hardness, the quinary  $\text{Mo}_{30}\text{Nb}_{35}\text{Ta}_5\text{V}_{25}\text{W}_5$  has also exhibited the highest yield strength and maximum compressive stress at  $1300^{\circ}\text{C}$ . Compared to a quinary alloy within the same MPEA alloy system reported in the literature,  $\text{Mo}_{21.7}\text{Nb}_{20.6}\text{Ta}_{15.6}\text{V}_{21}\text{W}_{21.1}$ , with a yield strength of 735MPa at  $1200^{\circ}\text{C}$  and 657MPa at  $1400^{\circ}\text{C}$ , the present  $\text{Mo}_{30}\text{Nb}_{35}\text{Ta}_5\text{V}_{25}\text{W}_5$  alloy has a lower yield strength of 466 MPa at  $1300^{\circ}\text{C}$ . However, the density of  $\text{Mo}_{30}\text{Nb}_{35}\text{Ta}_5\text{V}_{25}\text{W}_5$  (9.48 g/cm³) is also 20% lower than that of  $\text{Mo}_{21.7}\text{Nb}_{20.6}\text{Ta}_{15.6}\text{V}_{21}\text{W}_{21.1}$  (11.98 g/cm³) [31]. The quaternary alloys exhibit lower compressive yield strength

and maximum compression stress at both ambient temperature and  $1300^{\circ}\text{C}$  as compared to the quinary alloy. The quaternary alloy,  $\text{Mo}_{45}\text{Nb}_{35}\text{Ta}_5\text{V}_{15}$ , displays relatively low compressive yield strength and low maximum compressive strength at ambient as compared to other alloys. This is attributed to the high Mo content processing-induced defects. Molybdenum is prone to oxidation, and molybdenum oxide compounds have low evaporation temperatures [61,62]. These lead to weaker grain boundaries and the formation of very small porosity at grain boundaries due to evaporation of the oxides, leading to early failure. The compressive yield strengths and maximum stresses of the alloys are summarized in Table 2.

The HTP screening of yield strength indicates that the Mo<sub>30</sub>N $b_{35} Ta_5 V_{25} W_5$  alloy would possess the highest yield strength at  $1300^\circ C$  $(\sigma_{\rm YS}^{\rm HT}=428~{\rm MPa})$ . The measured yield strength at  $1300^{\circ}{\rm C}$  was  $\sigma_{\rm YS}^{\rm HT}=480$ MPa, a difference of +52 MPa.  $Mo_{45}Nb_{35}Ta_5V_{15}$  was predicted to have the second highest yield strength at  $1300^{\circ}$ C ( $\sigma_{VS}^{HT}$  383 MPa). The measured yield strength at 1300°C was 263 MPa, a difference of +120 MPa. Finally, the Mo<sub>25</sub>Nb<sub>50</sub>V<sub>20</sub>W<sub>5</sub> alloy was predicted to have a HT yield strength of 326 MPa and was observed to have a yield strength of 253 MPa, a difference of +73 MPa. It is important to note that not only did the HTP yield strength model accurately predict the yield strengths of the three candidate alloys (mean absolute error of 81.8 MPa, and root mean squared error of 86.7 MPa) but also correctly predicted the correct rank ordering of alloy according to yield strength. That is to say, the alloy with the highest predicted yield strength showed the highest experimental yield strength, and the alloy with the second highest predicted yield strength showed the second highest experimental yield strength, and so on. This further demonstrates the framework's capability for materials agnostic material design and optimization.

 Table 2

 A summary of all experimental and computational results generated for the three candidate alloys identified in this work. ROM: Rule of Mixtures.

	Nominal Composition	$\mathrm{Mo_{45}Nb_{35}Ta_5V_{15}}$	$Mo_{25}Nb_{50}V_{20}W_5$	$Mo_{30}Nb_{35}Ta_5V_{25}W_5$
As-Cast EL As-Cast EL Dendrite A Lattice Par Nanoinder Nanoinder Vickers Mi Vickers Mi Compressi Max. Com Compressi	As-Cast EDS (Whole Area, at. %)	Mo <sub>44.7</sub> Nb <sub>35.2</sub> Ta <sub>4.9</sub> V <sub>15.2</sub>	Mo <sub>24.5</sub> Nb <sub>49.8</sub> V <sub>20.8</sub> W <sub>4.9</sub>	Mo <sub>29.2</sub> Nb <sub>34.1</sub> Ta <sub>4.7</sub> V <sub>27.5</sub> W <sub>4.5</sub>
	As-Cast EDS (Dendrite only, at. %)	$Mo_{48.9}Nb_{34.1}Ta_{6.4}V_{10.6}$	$Mo_{28.1}Nb_{49.8}V_{14.5}W_{7.6}$	$Mo_{33.3}Nb_{32.8}Ta_{6.2}V_{20.2}W_{7.5}$
	As-Cast EDS (Inter-dendrite only, at. %)	$Mo_{26.9}Nb_{37.3}Ta_{2.4}V_{33.4}$	$Mo_{20.6}Nb_{49.9}V_{27.4}W_{2.1}$	$Mo_{17.6}Nb_{34.8}Ta_{2.4}V_{44.5}W_{0.7}$
	Dendrite Arm Spacing (µm)	$12.8~(\pm~4.8)$	15.1 ( $\pm$ 2)	$13.4~(\pm~2.2)$
	Lattice Parameter (nm)	BCC: 0.31813	BCC: 0.31604	BCC: 0.31779
	Nanoindentation Hardness (GPa)	6.86 ( $\pm$ 0.22)	6.85 ( $\pm$ 0.09)	7.20 ( $\pm$ 0.14)
	Nanoindentation Young's Modulus (GPa)	178 ( $\pm$ 6)	136 (± 3)	158 (± 4)
	Vickers Microhardness (HV) - As-cast	503 (± 9)	497 (± 7)	520 (± 8)
	Vickers Microhardness (HV) - Homogenized	$469 (\pm 14)$	477 (± 9)	480 (± 16)
	Compressive Yield Stress at RT (MPa)	752	974	1053
	Max. Compressive Stress at RT (MPa)	852	1210	1198
	Compressive Yield Stress at 1300°C (MPa)	263	253	480
	Max. Compressive Stress at 1300°C (MPa)	304	270	673
	Measured Density at RT (g/cc)	9.411	9.085	9.441
DFT	DFT Formation Enthalpy (meV-atom <sup>-1</sup> )	-117.4	-91.8	-99.3
	DFT Lattice Parameter (nm)	0.315	0.316	0.314
	DFT Young's Modulus (GPa)	186	147	173
	DFT Bulk Moduli (GPa)	210	193	201
	DFT Shear Moduli (GPa)	69	57	64
	DFT Estimated Yield Strength 1300°C (MPa)	290.0	230.86	270.6
High-Throughput Models	CALPHAD Phase (1300°C to Solidus)	BCC	BCC	BCC
	CALPHAD Solidus Temperature (K)	2804	2656	2699
	CALPHAD Liquidus Temperature	2830	2744	2790
	ROM Young's Modulus	1745	153	167
	ROM Bulk Modulus	197	190	194
	ROM Shear Modulus	64.70	56.14	61.6
	ROM Poisson Ratio	0.352	0.366	0.357
	Estimated Yield Strength 1300°C (MPa)	384	326	428
	CALPHAD RT Density (g/cc)	9.50	9.13	9.57
	CALPHAD ST Density (g/cc)	8.77	8.46	8.82

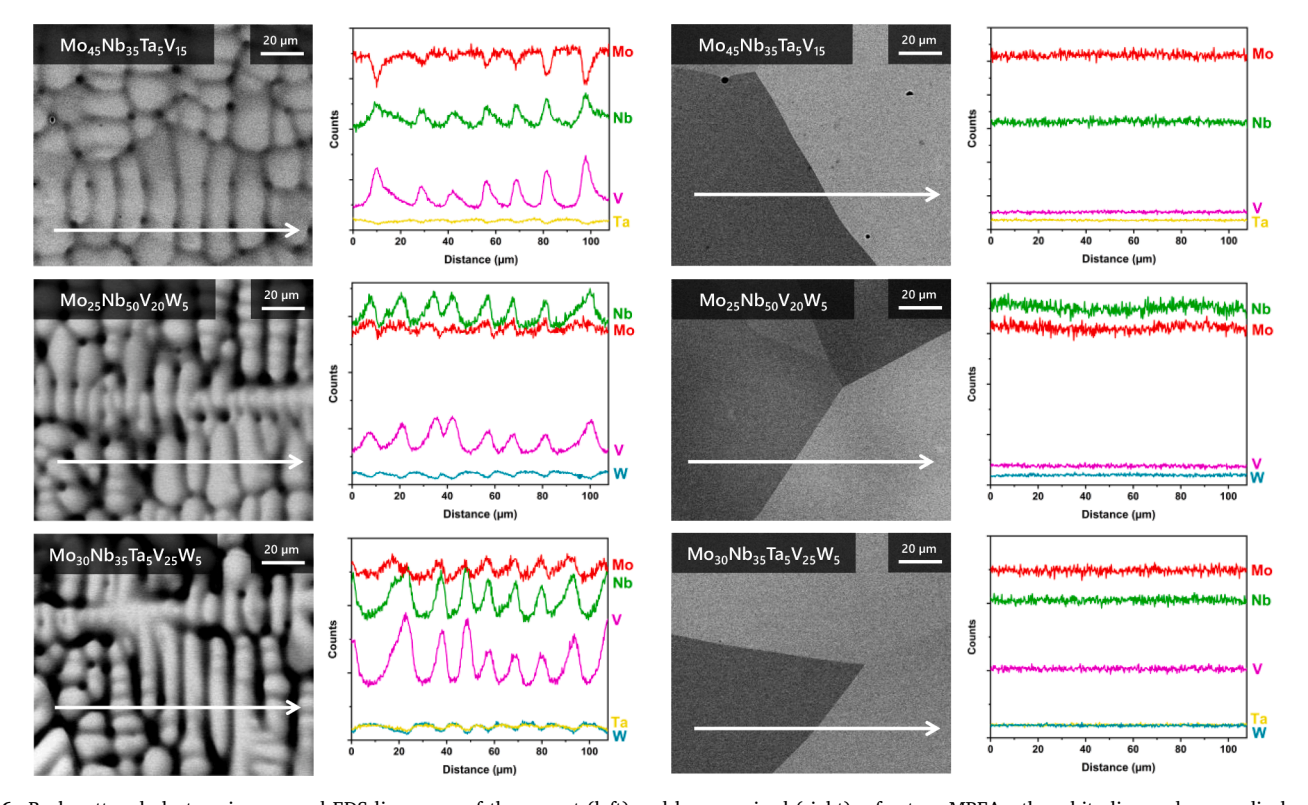


Fig. 6. Backscattered electron images and EDS line scans of the as-cast (left) and homogenized (right) refractory MPEAs; the white line and arrow displays the direction and the location of the line scan.

Selected Alloys Compared to Literature: Using a database of 1546 MPEAs curated by Borg et al. as a benchmark [63], we compare the measured and predicted properties of the 3 candidate alloys designed in

this work to values reported in the literature. With the composition-agnostic filtering approach used in this work, 468 single-phase BCC MPEAs were down-selected from 1546 MPEAs present

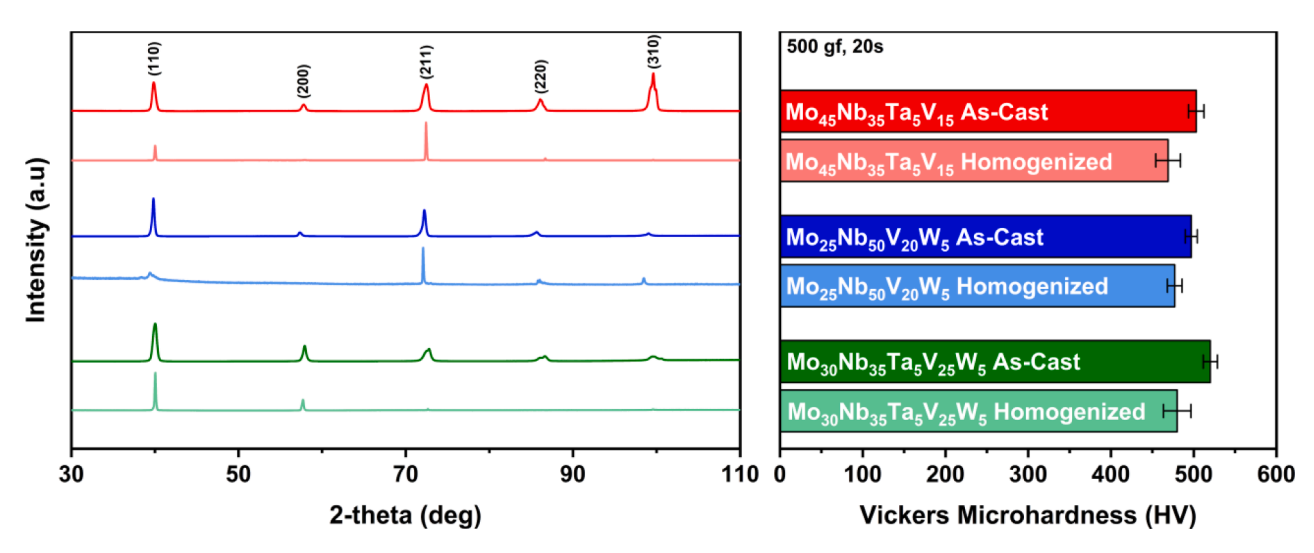


Fig. 7. XRD (left) and Vickers Microhardness (right) results for the three refractory MPEAs in this study were obtained from the as-cast and homogenized conditions.

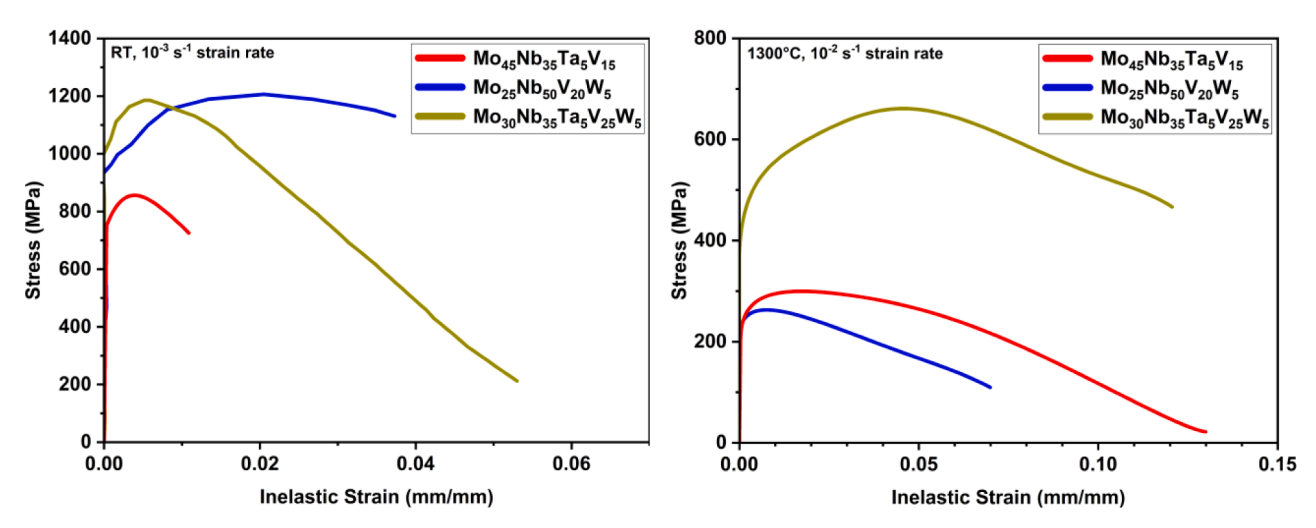


Fig. 8. Room temperature (left) and 1300°C (right) compressive engineering stress - inelastic strain curves for the three refractory MPEAs in this study in homogenized conditions.

in the database. Of these 468 single-phase BCC MPEAs, 348 MPEAs have yield strength data available. These 348 MPEAs are used to benchmark the 3 candidate alloys designed in this work.

The solidus temperature and density are known to be positively correlated, making the design of lightweight high-temperature alloys difficult. Fig. 9a depicts the predicted solidus temperature plotted against the predicted density near the melting point for 348 single-phase BCC refractory MPEAs. From Fig. 9a, a clear trade-off between lowdensity and high-temperature can be seen. Despite this, 6 alloys in the database simultaneously meet these constraints. In ascending order of density, these alloys are: MoNbTiV [64], Al<sub>0.25</sub>MoNbTiV [64], MoNbTi, MoNbTaTiV [29], Al<sub>0.2</sub>MoTaTiV [64], MoTaTiV [65]. All alloys except the three alloys designed in this work contain Ti. The lightest element comprising the 3 candidate alloys designed in this work is V (6.11 g/cc). Vanadium lowers the candidate alloy's density while simultaneously increasing the yield strength due to its large atomic mismatch within refractory MPEA lattices, which enhances solid solution strengthening. This indicates that, in addition to being an important alloying agent in refractory MPEAs for yield strength, V also has a critical role in reducing the density of refractory MPEAs.

Regarding yield strength, the yield strength of these 348 single-phase BCC refractory MPEAs are plotted against temperature in Fig. 9b. These alloys are then colored based on which constraint they fail; these

constraints are queried using the models listed in Table 1. Red points indicate a failure of the density constraint, blue points indicate a failure of the solidus constraint, and yellow points indicate a failure of the DBTT constraint. Failures of two constraints are indicated by purple, orange, and green; while failing of all constraints results in a black data point. The alloys that pass these 3 constraints are indicated by shapes outlined in black. The horizontal dashed line in Fig. 9b represents the 1300°C yield strength constraint. Many refractory MPEAs have measured yield strengths above 150 MPa at 1100°C; however, there are few measurements reported at temperatures greater than or equal to 1300°C. The few alloys that have been tested at temperatures greater than 1300°C are: HfMoNbTaTi [66], HfMoNbTaZr [66], MoNbTaVW [3], and MoNbTaW [8]. These alloys have exceptional high-temperature yield strength; however, they fail the density constraint. In fact, within this database of refractory MPEAs, there is a trade-off between high-temperature yield strength and density. This trade-off can be seen in Fig. 9b where alloys that have competitive high-temperature yield strength tend to fail the density constraint (depicted in red and purple).

Only 2 alloys (MoNbTi [28] and MoNbTaTiV [29]) of the initial 1546 data entries satisfy the DBTT, solidus, and density constraints. Of these passing data entries, none have had their yield strength tested beyond 1200°C, with the highest yield strength (MoNbTi) reported at 1200°C being 324 MPa, 156 MPa less than the best-performing alloy in this work

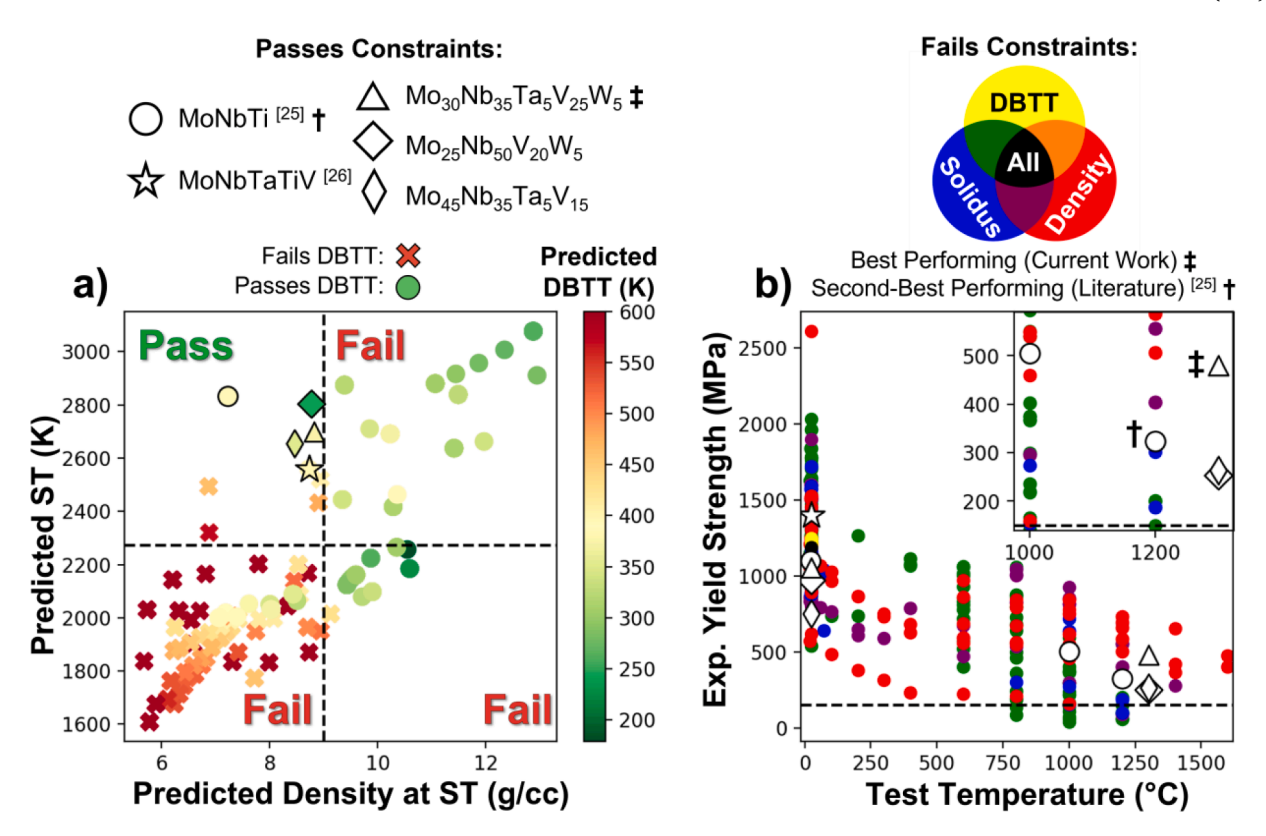


Fig. 9. A comparison between the 3 candidate alloys designed in this work with other refractory MPEAs with a single BCC phase reported in the literature. Of the initial 1546 MPEAs, only 468 are reported to be single-phase BCC and only 348 MPEAs having yield strength available. These 348 MPEAs are plotted to benchmark the designed alloy compositions. From these 348, the  $Mo_{30}Nb_{35}Ta_5V_{25}W_5$  alloy designed in this work is the strongest alloy that meets all relevant constraints. (a) The vertical and horizontal lines represent the density and solidus temperature constraints. Alloys that pass the density constraint tend to fail the solidus constraint, whereas alloys that pass the solidus constraint tend to fail the density constraint. (b) Alloys with high yield strength at high temperatures fail the density constraint. (ST: Solidus Temperature, Exp.: Experimental)

 $(Mo_{30}Nb_{35}Ta_5V_{25}W_5)$  that was tested at  $1300^{\circ}C.$  Furthermore, the MoNbTi alloy is predicted to have a higher melting temperature than the  $Mo_{30}Nb_{35}Ta_5V_{25}W_5$  alloy. Following the rule of thumb that the maximum operating temperature of an alloy is near 2/3 of  $T_s,\ MoNbTi$  would be expected to have a higher yield strength than  $Mo_{30}Nb_{35}Ta_5V_{25}W_5$  at the same temperature. This is not the case likely due to the higher configurational entropy and lattice mismatch of the  $Mo_{30}Nb_{35}Ta_5V_{25}W_5$  alloy, leading to improved yield strength at high temperature via solid solution strengthening.

## 5. Summary and conclusions

The design of novel structural materials for high-temperature applications in jet turbine engines cannot be myopic. However, to date, many works on the design of MPEAs make prescriptions about where in the MPEA space to explore prior to experimentation, or filter on a constraint that address a single property. In this work, we propose an alloy design framework that is composition agnostic, aware of multiple constraints, and leverages novel sampling techniques to select representative alloys of a down-selected feasible space. We first conduct an HTP composition agnostic factorial exploration of the WMoVTaNbAl MPEA space, simultaneously balancing multiple performance constraints to design an MPEA capable of operating in jet turbine engines. These performance constraints include: stability of a single BCC phase from 1300°C to the solidus temperature to ensure no undesired phases form during operation; a  $T_{solidus} > 2000^{\circ} C$  such that the candidate material is capable of reliably operating at 1300°C;  $\rho$  < 9 g/cc near solidus such that candidate alloys are lightweight;  $\sigma_{VS}^{HT} > 150$  MPa such that candidate alloys can withstand inherent operating stresses associated with the fast-rotating blades of jet turbines; and DBTT < 400 K such that the candidate alloys are sufficiently workable. When these 4 constraints relevant to the turbine blade application are considered within the WMoVTaNbAl MPEA space, only 0.54% of the alloy space remains feasible. This feasible space was found to be rich in Mo, Nb, and V and consisted of 214 alloys. Such a space is tractable for HTP computational analysis with DFT. Using a k-medoids based sampling scheme, 3 alloys were selected that best represent 3 regions in the feasible space.

The DFT analysis provided a thermodynamic and electronic assessment of the competitive properties associated with the downselected 218 MoNbV-rich alloys. These assessments include phase stability and short-range order associated with the resultant MoNbV-rich feasible space. The DFT-queried Eform indicates that the presence of V increases the solubility limit of Mo in MPEAs. Furthermore, both DFT-queried Eform and B indicate increasing Mo and V content increase the likelihood of having a high yield strength. The DFT-calculated structural properties, such as lattice parameters, elastic constants, and misfit volumes combined with the Curtin-Maresca model, indicate that, within this feasible space of alloys, optimally strong alloys contain a concentration of V ranging from 15-25 at.%, in agreement with other works where 1) V was determined to be the most potent alloving agent for strengthening and 2) the optimal composition of V for strengthening is 20-25 at.% [51]. Furthermore, the SRO analysis of the three representative alloys predicts that the three alloys designed in this work maintain a single-phase BCC with high yield strength at 1300°C, which was confirmed by the experiments.

Finally, three representative alloys were synthesized and characterized to validate whether the proposed alloys indeed meet the constraints specified at the beginning of the alloy design campaign. All three alloys exhibit a single BCC phase after heat treatments, in agreement with CALPHAD predictions and SRO analysis. The RT density of the alloys

was determined to be less than 9.5 g/cc, comparable to Ni-based superalloys. Furthermore, these observed densities are in close agreement with CALPHAD predictions. All alloys exhibited compressive yield strengths at  $1300^{\circ}\text{C}$  above the 150 MPa constraint, according to the predictions from the DFT-informed Curtin-Maresca Model. When compared to the literature, only two alloys, MoNbTi [28] and MoNbTaTiV [29], meet the constraints applied in this work. Of these two alloys, only MoNbTi [28] is tested at high temperature. The yield strength of the strongest alloy designed in this work,  $Mo_{30}\text{Nb}_{35}\text{Ta}_5\text{V}_{25}\text{W}_5$ , is 156 MPa higher at  $1300^{\circ}\text{C}$  than MoNbTi [28] tested at  $1200^{\circ}\text{C}$ , showing that  $Mo_{30}\text{Nb}_{35}\text{Ta}_5\text{V}_{25}\text{W}_5$  out performs MoNbTi regarding the HT yield strength.

Based on these computational and experimental results, we conclude that the proposed design scheme identifies candidate alloys that are likely to be promising for applications in jet turbine engines. It was observed that when application-relevant constraints are applied to the WMoVTaNbAl MPEA space, only0.54% of the original design space remains feasible, lending support to the adage, "the high-entropy alloy space is not as big as we think it is" [67]. Therefore, MoNbV-rich MPEAs merit further consideration when designing next-generation structural materials for jet turbine engines.

## **Declaration of Competing Interest**

The authors declare that they have no known competing financial interests or personal relationships that could have appeared to influence the work reported in this paper.

#### Acknowledgements

The authors acknowledge the support from the U.S. Department of Energy (DOE) ARPA-E ULTIMATE Program through Project DE-AR0001427. TK and BV acknowledge the support of NSF through Grant no. DGE-1545403. BV acknowledges the support of NSF through Grant no. 1746932. RA acknowledges the support from Grants no. NSF-CISE-1835690 and NSF-DMREF-2119103. IK and CA acknowledge support from the NASA ESI Program through Grant No. 80NSSC21K0223. Specific applications of electronic-structure theory (PS and DDJ) at Ames Laboratory were supported by the DOE ARPA-E ULTIMATE Program, while the U.S. DOE supported the theory developments at Ames Laboratory, Office of Science, Basic Energy Sciences, Materials Science and Engineering Department. Ames Laboratory is operated by Iowa State University for the U.S. DOE under contract DE-AC02-07CH11358. High-throughput CALPHAD calculations were carried out partly at the Texas A&M High-Performance Research Computing (HPRC) Facility.

# Supplementary materials

Supplementary material associated with this article can be found, in the online version, at doi:10.1016/j.actamat.2023.118784.

# References

- [1] J. Rame, S. Utada, L.M. Bortoluci Ormastroni, L. Mataveli-Suave, E. Menou, L. Després, P. Kontis, J. Cormier, Platinum-containing new generation nickel-based superalloy for single crystalline applications, Superalloys 2020 (2020) 71–81. Springer.
- [2] T.M. Pollock, Alloy design for aircraft engines, Nat. Mater. 15 (8) (2016) 809–815.
- [3] O.N. Senkov, D.B. Miracle, K.J. Chaput, J.-P. Couzinie, Development and exploration of refractory high entropy alloys-a review, J. Mater. Res. 33 (19) (2018) 3092–3128.
- [4] D.B. Miracle, O.N. Senkov, A critical review of high entropy alloys and related concepts. Acta Mater. 122 (2017) 448–511.
- [5] M.H. Tsai, J.W. Yeh, High-entropy alloys: a critical review, Mater. Res. Lett. 2 (3) (2014) 107–123
- [6] S. Gorsse, D.B. Miracle, O.N. Senkov, Mapping the world of complex concentrated alloys, Acta Mater. 135 (2017) 177–187.
- [7] M. Dada, P. Popoola, S. Adeosun, N. Mathe, High entropy alloys for aerospace applications, Aerodynamics (2019).

[8] O.N. Senkov, G.B. Wilks, J.M. Scott, D.B. Miracle, Mechanical properties of Nb25Mo25Ta25W25 and V20Nb20Mo20Ta20W20 refractory high entropy alloys, Intermetallics 19 (5) (2011) 698–706.

- [9] J. Chen, X. Zhou, W. Wang, B. Liu, Y. Lv, W. Yang, D. Xu, Y. Liu, A review on fundamental of high entropy alloys with promising high-temperature properties, J. Alloy. Compd. 760 (2018) 15–30.
- [10] Y.L. Hu, L.H. Bai, Y.G. Tong, D.Y. Deng, X.B. Liang, J. Zhang, Y.J. Li, Y.X. Chen, First-principle calculation investigation of NbMoTaW based refractory high entropy alloys, J. Alloy. Compd. 827 (2020), 153963.
- [11] S. Ge, H. Fu, L. Zhang, H. Mao, H. Li, A. Wang, W. Li, H. Zhang, Effects of Al addition on the microstructures and properties of MoNbTaTiV refractory high entropy alloy, Mater. Sci. Eng. A 784 (2020), 139275.
- [12] Y. Long, X. Liang, K. Su, H. Peng, X. Li, A fine-grained NbMoTaWVCr refractory high-entropy alloy with ultra-high strength: microstructural evolution and mechanical properties, J. Alloy. Compd. 780 (2019) 607–617.
- [13] Z.D. Han, N. Chen, S.F. Zhao, L.W. Fan, G.N. Yang, Y. Shao, K.F. Yao, Effect of Ti additions on mechanical properties of NbMoTaW and VNbMoTaW refractory high entropy alloys, Intermetallics 84 (2017) 153–157.
- [14] O.N. Senkov, C. Woodward, D.B. Miracle, Microstructure and properties of aluminum-containing refractory high-entropy alloys, JOM 66 (10) (2014) 2030, 2042
- [15] A.B. Kustas, M.R. Jones, F.W. DelRio, P. Lu, J. Pegues, P. Singh, A.V. Smirnov, J. Tiarks, E.D. Hintsala, D.D. Stauffer, J.K. Román-Kustas, M. Abere, E.M.H. White, D.D. Johnson, I.E. Anderson, N. Argibay, Extreme hardness at high temperature with a lightweight additively manufactured multi-principal element superalloy, Appl. Mater. Today 29 (2022), 101669.
- [16] X. Li, H. Li, Q. Li, C. Jin, K. Hua, H. Wang, The determining role of Al addition on tribology properties and oxidation behavior at elevated temperatures of TiZrHfNb refractory high-entropy alloy, Mater. Charact. 189 (2022), 111921.
- [17] Z. Li, W. Lai, B. Wang, X. Tong, D. You, W. Li, X. Wang, A novel Ti42.5Zr42.5Nb5Ta10 multi-principal element alloy with excellent properties for biomedical applications. Intermetallics 151 (2022), 107731.
- [18] Z. Guo, A. Zhang, J. Han, J. Meng, Effect of Si additions on microstructure and mechanical properties of refractory NbTaWMo high-entropy alloys, J. Mater. Sci. 54 (7) (2019) 5844–5851.
- [19] V. Bhardwaj, Q. Zhou, F. Zhang, W. Han, Y. Du, K. Hua, H. Wang, Effect of Al addition on the microstructure, mechanical and wear properties of TiZrNbHf refractory high entropy alloys, Tribol. Int. 160 (2021), 107031.
- [20] B. Chen, S. Li, H. Zong, X. Ding, J. Sun, E. Ma, Unusual activated processes controlling dislocation motion in body-centered-cubic high-entropy alloys, Proc. Natl. Acad. Sci. 117 (28) (2020) 16199–16206.
- [21] F. Wang, G.H. Balbus, S. Xu, Y. Su, J. Shin, P.F. Rottmann, K.E. Knipling, J. C. Stinville, L.H. Mills, O.N. Senkov, I.J. Beyerlein, T.M. Pollock, D.S. Gianola, Multiplicity of dislocation pathways in a refractory multiprincipal element alloy, Science 370 (6512) (2020) 95–101.
- [22] O.A. Waseem, U. Auyeskhan, H.M. Lee, H.J. Ryu, A combinatorial approach for the synthesis and analysis of AlxCryMozNbTiZr high-entropy alloys: oxidation behavior, J. Mater. Res. 33 (19) (2018) 3226–3234.
- [23] R. Feng, C. Zhang, M.C. Gao, Z. Pei, F. Zhang, Y. Chen, D. Ma, K. An, J. D. Poplawsky, L. Ouyang, Y. Ren, J.A. Hawk, M. Widom, P.K. Liaw, Highthroughput design of high-performance lightweight high-entropy alloys, Nat. Commun. 12 (1) (2021) 4329.
- [24] P. Singh, A. Sharma, A.V. Smirnov, M.S. Diallo, P.K. Ray, G. Balasubramanian, D. D. Johnson, Design of high-strength refractory complex solid-solution alloys, NPJ Comput. Mater. 4 (1) (2018) 16.
- [25] T.Z. Khan, T. Kirk, G. Vazquez, P. Singh, A.V. Smirnov, D.D. Johnson, K. Youssef, R. Arróyave, Towards stacking fault energy engineering in FCC high entropy alloys, Acta Mater. 224 (2022), 117472.
- [26] T.S. Madhulatha, Comparison between k-means and k-medoids clustering algorithms, in: Proceedings of the International Conference on Advances in Computing and Information Technology, Springer, 2011, pp. 472–481.
- [27] K. Crombecq, I. Couckuyt, D. Gorissen, T. Dhaene, Space-filling sequential design strategies for adaptive surrogate modelling, in: Proceedings of the First International Conference on Soft Computing Technology in Civil, Structural and Environmental Engineering, 2009.
- [28] O.N. Senkov, S. Gorsse, D.B. Miracle, High temperature strength of refractory complex concentrated alloys, Acta Mater. 175 (2019) 394–405.
- [29] H.W. Yao, J.W. Qiao, J.A. Hawk, H.F. Zhou, M.W. Chen, M.C. Gao, Mechanical properties of refractory high-entropy alloys: experiments and modeling, J. Alloy. Compd. 696 (2017) 1139–1150.
- [30] Thermo-Calc, TCHEA: high entropy alloys database version 4.1. June 2020. https://thermocalc.com/blog/thermo-calc-2020b-is-released/, 2020).
- [31] F. Maresca, W.A. Curtin, Mechanistic origin of high strength in refractory BCC high entropy alloys up to 1900K, Acta Mater. 182 (2020) 235–249.
- [32] D.D. Johnson, D.M. Nicholson, F.J. Pinski, B.L. Gyorffy, G.M. Stocks, Density-functional theory for random alloys: total energy within the coherent-potential approximation, Phys. Rev. Lett. 56 (19) (1986) 2088–2091.
- [33] D.D. Johnson, F.J. Pinski, Inclusion of charge correlations in calculations of the energetics and electronic structure for random substitutional alloys, Phys. Rev. B 48 (16) (1993) 11553–11560.
- [34] A. Alam, D.D. Johnson, Structural properties and relative stability of (meta)stable ordered, partially ordered, and disordered Al-Li alloy phases, Phys. Rev. B 85 (14) (2012), 144202.
- [35] M.A.L. Marques, M.J.T. Oliveira, T. Burnus, Libxc: a library of exchange and correlation functionals for density functional theory, Comput. Phys. Commun. 183 (10) (2012) 2272–2281.

- [36] H.J. Monkhorst, J.D. Pack, Special points for Brillouin-zone integrations, Phys. Rev. B 13 (12) (1976) 5188–5192.
- [37] P. Singh, A.V. Smirnov, D.D. Johnson, Atomic short-range order and incipient long-range order in high-entropy alloys, Phys. Rev. B 91 (22) (2015), 224204.
- [38] R. Zhang, S. Zhao, J. Ding, Y. Chong, T. Jia, C. Ophus, M. Asta, R.O. Ritchie, A. M. Minor, Short-range order and its impact on the CrCoNi medium-entropy alloy, Nature 581 (7808) (2020) 283–287.
- [39] T. Mukherjee, J.S. Zuback, A. De, T. DebRoy, Printability of alloys for additive manufacturing, Sci. Rep. 6 (1) (2016) 19717.
- [40] P. Singh, S. Gupta, S. Thimmaiah, B. Thoeny, P.K. Ray, A.V. Smirnov, D. D. Johnson, M.J. Kramer, Vacancy-mediated complex phase selection in high entropy alloys, Acta Mater. 194 (2020) 540–546.
- [41] P. Singh, S. Picak, A. Sharma, Y.I. Chumlyakov, R. Arroyave, I. Karaman, D. D. Johnson, Martensitic transformation in Fe<sub>x</sub>Mn<sub>80-x</sub>Co<sub>10</sub>Cr<sub>10</sub> high-entropy alloy, Phys. Rev. Lett. 127 (11) (2021), 115704.
- [42] T. Kirk, B. Vela, S. Mehalic, K. Youssef, R. Arróyave, Entropy-driven melting point depression in fcc HEAs, Scr. Mater. 208 (2022), 114336.
- [43] D. Khatamsaz, B. Vela, P. Singh, D.D. Johnson, D. Allaire, R. Arróyave, Multiobjective materials bayesian optimization with active learning of design constraints: Design of ductile refractory multi-principal-element alloys, Acta Mater. 236 (2022) 118133
- [44] L. Van der Maaten, G. Hinton, Visualizing data using t-SNE, J. Mach. Learn. Res. 9 (11) (2008).
- [45] L. McInnes, J. Healy, J. Melville, Umap: Uniform manifold approximation and projection for dimension reduction, arXiv preprint arXiv:1802.03426 (2018).
- [46] G.B. Olson, Designing a new material world, Science 288 (5468) (2000) 993–998.
- [47] P. Pandey, N. Mazumder, M.P. Singh, C. Patil, A. Sharma, S.K. Makineni, D. Banerjee, K. Chattopadhyay, Design of low mass density γ/γ' CoNi-based superalloys with promising high-temperature mechanical properties, Phys. Rev. Mater. 5 (9) (2021), 093601.
- [48] T. Kobayashi, Advances in turbine materials design and manufacturing, in: Proceedings of the 4th International Charles Parsons Turbine Conference, Newcastle upon Tyne, 1997, p. 766.
- [49] T. Yokokawa, H. Harada, K. Kawagishi, T. Kobayashi, M. Yuyama, Y. Takata, Advanced Alloy Design Program and Improvement of Sixth-Generation Ni-Base Single Crystal Superalloy TMS-238, in: S. Tin, M. Hardy, J. Clews, J. Cormier, Q. Feng, J. Marcin, C. O'Brien, A. Suzuki (Eds.) Superalloys 2020, Springer International Publishing, Cham, 2020, pp. 122-130.
- [50] ULTIMATE | arpa-e.energy.gov.
- [51] B. Yin, F. Maresca, W.A. Curtin, Vanadium is an optimal element for strengthening in both fcc and bcc high-entropy alloys, Acta Mater. 188 (2020) 486–491.

- [52] R. Singh, A. Sharma, P. Singh, G. Balasubramanian, D.D. Johnson, Accelerating computational modeling and design of high-entropy alloys, Nat. Comput. Sci. 1 (1) (2021) 54–61.
- [53] D. Rodney, L. Ventelon, E. Clouet, L. Pizzagalli, F. Willaime, Ab initio modeling of dislocation core properties in metals and semiconductors, Acta Mater. 124 (2017) 633–659.
- [54] Y. Song, R. Yang, D. Li, W.T. Wu, Z.X. Guo, Calculation of theoretical strengths and bulk moduli of bcc metals, Phys. Rev. B 59 (22) (1999) 14220–14225.
- [55] G. Vazquez, P. Singh, D. Sauceda, R. Couperthwaite, N. Britt, K. Youssef, D. D. Johnson, R. Arróyave, Efficient machine-learning model for fast assessment of elastic properties of high-entropy alloys, Acta Mater. 232 (2022), 117924.
- [56] D. Beniwal, P. Singh, S. Gupta, M.J. Kramer, D.D. Johnson, P.K. Ray, Distilling physical origins of hardness in multi-principal element alloys directly from ensemble neural network models, npj, Comput. Mater. 8 (1) (2022) 153.
- [57] B. Zhang, Y. Mu, M.C. Gao, W.J. Meng, S.M. Guo, On single-phase status and segregation of an as-solidified septenary refractory high entropy alloy, MRS Commun. 7 (1) (2017) 78–83.
- [58] P.E. Blackburn, M. Hoch, H.L. Johnston, The vaporization of molybdenum and tungsten oxides, J. Phys. Chem. 62 (7) (1958) 769–773.
- [59] M. Regenberg, G. Hasemann, M. Wilke, T. Halle, M. Krüger, Microstructure evolution and mechanical properties of refractory Mo-Nb-V-W-Ti high-entropy alloys, Metals 10 (11) (2020) 1530.
- [60] H. Yao, J.W. Qiao, M.C. Gao, J.A. Hawk, S.G. Ma, H. Zhou, MoNbTaV mediumentropy alloy, Entropy 18 (5) (2016) 189.
- [61] G.R. Smolik, D.A. Petti, S.T. Schuetz, Oxidation and volatilization of TZM alloy in air, J. Nucl. Mater. 283-287 (2000) 1458-1462.
- [62] T. Fu, F. Shen, Y. Zhang, L. Yu, K. Cui, J. Wang, X. Zhang, Oxidation protection of high-temperature coatings on the surface of Mo-based alloys-A Review, Coatings 12 (2) (2022), 141.
- [63] C.K.H. Borg, C. Frey, J. Moh, T.M. Pollock, S. Gorsse, D.B. Miracle, O.N. Senkov, B. Meredig, J.E. Saal, Expanded dataset of mechanical properties and observed phases of multi-principal element alloys, Sci. Data 7 (1) (2020) 430.
- [64] S.Y. Chen, X. Yang, K.A. Dahmen, P.K. Liaw, Y. Zhang, Microstructures and crackling noise of AlxNbTiMoV high entropy alloys, Entropy 16 (2) (2014) 870–884.
- [65] D.X. Qiao, H. Jiang, X.X. Chang, Y.P. Lu, T.J. Li, Microstructure and mechanical properties of VTaTiMoAlx refractory high entropy alloys, Materials. Sci. Forum (2017) 638–642. Trans Tech Publ.
- [66] K.K. Tseng, C.C. Juan, S. Tso, H.C. Chen, C.W. Tsai, J.W. Yeh, Effects of Mo, Nb, Ta, Ti, and Zr on mechanical properties of equiatomic Hf-Mo-Nb-Ta-Ti-Zr alloys, Entropy (2019).
- [67] R. Arroyave, The high entropy alloy space is not as big as we think it is, Youtube, 2021.